ISTANBUL TECHNICAL UNIVERSITY ★ GRADUATE SCHOOL OF SCIENCE
ENGINEERING AND TECHNOLOGY

DEVELOPMENT OF NEW GENERATION FE - BASED AL - SI - MO ALLOYS FOR EXHAUST MANIFOLD APPLICATIONS

M.Sc. THESIS

Rıfat YILMAZ

Department of Metallurgical & Materials Engineering

Materials Engineering Programme

MAY, 2014

ISTANBUL TECHNICAL UNIVERSITY ★ GRADUATE SCHOOL OF SCIENCE
ENGINEERING AND TECHNOLOGY

DEVELOPMENT OF NEW GENERATION FE - BASED AL - SI - MO ALLOYS FOR EXHAUST MANIFOLD APPLICATIONS

M.Sc. THESIS

Rıfat YILMAZ
(506121420)

Department of Metallurgical & Materials Engineering

Materials Engineering Programme

Thesis Advisor: Asst. Prof. Dr. Nuri SOLAK

MAY, 2014

İSTANBUL TEKNİK ÜNİVERSİTESİ ★ FEN BİLİMLERİ ENSTİTÜSÜ

EGZOZ MANİFOLD UYGULAMALARI İCİN YENİ NESİL AL - SI - MO ALAŞIMLI DOKME DEMİRLERİN GELİŞTİRİLMESİ

YÜKSEK LİSANS TEZİ

Rıfat YILMAZ
(506121420)

Metalurji ve Malzeme Mühendisliği Anabilim Dalı

Malzeme Mühendisliği Programı

Tez Danışmanı: Asst. Prof. Dr. Nuri SOLAK

MAYIS, 2014

Rıfat YILMAZ, a M.Sc. student of ITU Graduate School of Science Engineering and Technology 506121420 successfully defended the thesis entitled **“DEVELOPMENT OF NEW GENERATION FE - BASED AL - SI - MO ALLOYS FOR EXHAUST MANIFOLD APPLICATIONS”**, which he/she prepared after fulfilling the requirements specified in the associated legislations, before the jury whose signatures are below.

Thesis Advisor : **Asst. Prof. Dr. Nuri SOLAK** ....
Istanbul Technical University

Jury Members : **Asst. Prof. Dr. Nuri SOLAK** ....
Istanbul Technical University

Prof. Dr. Mustafa Kamil ÜRGEN ....
Istanbul Technical University

Assoc. Prof. Dr. Özgür BİRER ....
Koç University

Date of Submission : **05 May 2014**
Date of Defense : **29 May 2014**

To my Mom and Dad,

FOREWORD

"This complicated array of moving things which constitutes ***the world*** *is something like a great chess game being played by the gods, and we are observers of the games. We do not know what the rules of the game are; all we are allowed to do is to watch the playing. If we know the rules, we consider that we* ***understand*** *the world."*

– Richard Phillips Feynman.

Humankind's relationship with iron is currently believed to cover at least seven millennia. How many times have I heard the question *"Is there still anything to discover in cast iron?"*, often ends of the conversation continued in *"We know everything about cast irons - they've been studied for years!* On the contrary, in recent decades, more than half of the cast irons used in today did not exist fifteen years ago. In this study, High aluminum, silicon and molybdenum containing cast irons for hot end exhaust system applications is investigated and will be presented.

I am truly grateful to my adviser Asst. Prof. Dr. Nuri SOLAK for his invaluable guidance, encouragement and kind support during the whole study. I am very thankful to Prof. Dr. Mustafa ÜRGEN for his professional advices and definite support.

Additionally, I would like to thank my friend and colleague Emin KONDAKÇI for his generous support and encouragement throughout the project. I am thankful to Ahmet Fatih YAYLA, Barış YAVAŞ, Çağatay YELKARASI and Oğuzkaan ÇOŞKUN for their interest and help during micro-hardness, TG/DTA, XRD, SEM/EDS characterization of samples and conducting thermal fatigue test, respectively. Also, I would like to thank Salih DEMIRSOY from Demirsoy Foundry for casting of materials. I mostly appreciate support and help from my colleagues in Solak Group, ITU.

Special thanks to Assoc. Prof. Dr. Oğuzhan GÜRLÜ for him professional advices and supporting me for all time.

Finally, I would like to thank to my family and Gülçin UYGUR for their unconditional love, great support and advices in all domains.

May, 2014

Rıfat YILMAZ
Physics Engineer

TABLE OF CONTENTS

Page

ABBREVIATIONS

A1 : Eutectoid Phase Transition Temperature
AlSiMo : Aluminum containing High Si-Mo Cast Iron
Al_2SiO_5 : Aluminasilicate
CALPHAD : Calculation of Phase Diagrams
CGI : Compacted Graphite Iron
EDS : Electron Disperve Spectroscopy
Fe_2O_3 : Hematite
$FeAl_2O_4$: Ironaluminate
GDOES : Glow Discharge Optic Emission Spectroscopy
IP : In-Phase
OP : Out-of-Phase
SEM : Scanning Electron Microscope
SGTE : Scientific Group Thermodata Europe
TMF : Thermo-Mechanical Fatigue
TG/DTA :Thermogravimetric and Differential Thermal Analysis
XRD : X-ray Difractometre

LIST OF TABLES

LIST OF FIGURES

Page

DEVELOPMENT OF NEW GENERATION FE - BASED AL - SI - MO ALLOYS FOR EXHAUST MANIFOLD APPLICATIONS

SUMMARY

Thermal stresses of exhaust manifolds have increased significantly in the last two decades. Nowadays, to raise the engine performance and overall efficiency is the most encountered challenge for the automotive industry, and at the same time, customer's expectation for safety, fuel economy and price would be fulfilled. Increasing efficiency and the new demands regarding the emissions causes the exhaust gas temperatures to increase. Considering all these demands on hot end exhaust systems, it is aimed that while increasing the high temperature oxidation, creep and fatigue resistance, it is intended to improve engine performance, reduce weight, and also increase the cost efficiency. In this study, Fe-based AlSiMo cast alloys for engine exhaust manifolds application are investigated by adding aluminum and reducing molybdenum content in High Si - Mo cast iron. High temperature oxidation behavior, thermal fatigue resistance and thermodynamics properties of AlSiMo alloys are studied by computationally and experimentally. By adding aluminum to the High Si - Mo cast iron, temperature of eutectoidic phase transformation in the Fe-C system is increased. Therefore, the expansions resulting from transformation of crystal structure is deferred to high temperatures and the possibility of thermal fatigue induced crack growth is reduced. Also, it is observed that high temperature oxidation behavior of AlSiMo alloys is directly connected with content of aluminum. High temperature oxidation tests are performed at elevated temperatures. SEM, EDS, XRD and GDOES measurements are carried out on samples for detecting oxide phases and oxide scale thickness and microstructural analysis. Additionally, thermal fatigue tests are conducted at 850^oC, and aluminum containing High Si-Mo alloys show better thermal fatigue resistance. It is observed that the crack initiation defers to higher thermal cycles.

To conclude, it is resulted with this study that selective diffusion and oxidation of aluminum at the surface is observed which improves the oxidation resistance of AlSiMo alloys. Addition to this, aluminum containing High Si-Mo alloys exhibit more thermal fatigue resistance than High Si-Mo cast irons.

EGZOZ MANİFOLD UYGULAMALARI İCİN YENİ NESİL AL - SI - MO ALAŞIMLI DOKME DEMİRLERİN GELİŞTİRİLMESİ

ÖZET

Otomotiv endüstrisi son yıllarda; yasal düzenlemelerin, çevresel kaygıların ve global ölçekli yüksek rekabetin etkisiyle her geçen gün daha çetin şartlar ve problemlerle karşı karşıya kalmaktadır. Müşteri beklentilerini karşılayabilen, yüksek performansı ekonomik şartlarda sağlayabilen, yasal düzenlemeler ile belirlenmiş güvenlik ve emisyon seviyelerini yakalayabilen yeni nesil araçların üretimi gün geçtikçe sektörü daha ileri teknoloji alanlarında araştırmalar ve yatırımlar yapmaya zorlamaktadır. Bunların yanında düşük maliyet, hafiflik, sessiz çalışma ve konfor gibi ikincil ve rekabetçi hedefler de sektörü yeni çalışmalara itmektedir. Bu hedefler araç motorlarında yapılan tasarım değişiklikleri, iç basınçlar ve sıcaklıkları gibi performansı doğrudan etkileyen çalışma şartlarının limitlere çekilmesi ve istatistiksel araştırmaların ışığında emniyet katsayılarının düşürülmesi ile büyük ölçüde tutturulmuştur. Diğer bir yandan da bu hedeflerin tutturulması, içten yanmalı motorların maruz kaldığı zorlanmaların büyüklüklerini arttırmış ve çeşitlendirmiştir. özellikle iç basınçların ve sıcaklıkların arttırılması motor parçalarının daha fazla zorlanmasına sebep olmaktadır. Bu zorlanmaların en önemlilerinin ikisi de termal yorulma ve termomekanik yorulma fenomenleridir. Müşterinin kullanım şartları, aracın kullanıldığı çevrenin koşulları ve aracın kullanıldığı yol şartları içten yanmalı motorların termal ve termomekanik çevrimlere maruz kalmasına sebep olur. Artan basınç ve sıcaklıklar ile bu çevrimlerde ulaşılan azami sıcaklık ve basınç değerleri daha da artmıştır ve bu yorulmalar motor komponentlerini daha da hızlı bir şekilde hasara zorlamaktadır. özellikle yüksek basınç ve sıcaklıklara doğrudan maruz kalan, herhangi bir şekilde soğutma sistemine sahip olmayan ve karmaşık geometrileri dolayısıyla döküm üretim yöntemiyle üretilen egzoz manifold parçaları, turboşarj ünitesi muhafaza parçaları ve döküm egzoz boruları termal ve termomekanik yorulmaya ciddi şekilde maruz kalmaktadır. Bu zorlanmalara karşı daha dayanıklı tasarım elde etmek için et kalınlıklarının arttırılması, parçalara kaplama yapılması veya farklı soğutma yöntemlerinin parçalara entegre edilmesi gibi çözümler uygulanmıştır. Ancak bu yöntemler aracın ağırlığını arttırması, yakıt tüketim performansı düşürmesi, egzoz emisyon seviyelerini yükseltmesi ve üretim maliyetlerini ve karmaşıklıklarını arttırması sebebiyle yetersiz kalmaktadır. Şüphesiz ki bu noktadan sonra yapılması gereken en önemli geliştirme bahsi geçen komponentlerin üretiminde kullanılan malzemelerin geliştirilmesidir.

Günümüz otomotiv araçlarının içten yanmalı motorları için üretilen egzoz manifoldu, turboşarj muhafazası gibi yüksek sıcaklığa maruz kalan parçaların büyük çoğunluğu küresel grafitli dökme demir, daha nadir olarak ise gri dökme demir, vermiküler dökme demirden üretilmektedir. İçten yanmalı motorlardaki egzoz gazı sıcaklıklarının artışı ile birlikte yüksek sıcaklık dayanımı daha gelişmiş olan Silisyum ve Molibden katkılı yüksek alaşımlı küresel dökme demirler, yüksek Nikel katkılı dökme demirler

ve paslanmaz çelikler motorun sıcak çalışan komponentleri için sektördeki ana malzemeler halinde gelmiştir. Bu malzemeler dış ülkelere olan bağımlılık ve yüksek maliyetlerinden dolayı ülkemiz otomotiv endüstrisi için ideal malzemeler değillerdir. özellikle nikel üretimi ülkemizde yoktur. Bu koşulların oluşması muhakkak ki; malzeme teknolojileri üzerine araştırma yapılması için uygun zemine sebep olmuştur. Yüksek ısıya karşı daha dayanıklı olan ve maliyetleri Nikel ve Molibden gibi madenlerin getirdiği maliyetlere göre çok daha düşük olan bir dökme demir geliştirilmesi, yukarıda bahsedilen problemlerin çözümüne çok büyük bir katkı sağlayacaktır. Geliştirilecek yeni dökme demir malzemesi sayesinde istenilen dayanıma sahip komponentlerin üretimi düşük maliyetli bir şekilde yapılabilmesi ve dışa bağımlılığın önüne geçilmesi hedeflenmektedir. Buna ek olarak da içten yanmalı motorda herhangi bir ağırlık artışı, yakıt tüketimi artışı ve emisyon iyileştirme performansında azalma meydana gelmemesi hedeflenmektedir.

Bu çalışmada yüksek silisyum - molibden içeren küresel grafitli dökme demirlere aluminyum eklenerek yeni nesil yüksek aluminyum-silisyum-molibden içeren dökme demirler geliştirilmiştir. Bu çalışma boyunca termodinamik hesaplamalar ve deneysel çalışmalar yapılmış; AlSiMo alaşımların termo-kimyasal, termo-fiziksel ve termo-mekanik davranışları araştırılmıştır. Termodinamik hesaplamalar CALPHAD yaklaşımı kullanılarak yapılmıştır. Hesaplamalı faz denge diagramları kısaca CALPHAD yaklaşımı Gibbs Enerji minimizasyon yöntemini kullanarak her bir komponentin tüm fazları için termodinamik denge hesaplar. Tüm bu hesaplamalar sıcaklık, kompozisyon ve basınç gibi değişkenler üzerinden ifade edilebilir. Calphad yöntemi teori ile deney arasında bir köprü vazifesi görmektedir. Her iki bileşenden de girdiler alıp, en hassas ve doğru olan çözüme ulaşmayı hedefler. Bu çalışmada yapılan tüm hesaplamalar; Calphad yöntemini kullanan Thermo-Calc yazılımı ile yapılmıştır. Veritabanı olarak ise SGTE, TCFE6, ve SSOL5 kullanılmıştır. Bu sayede multi-komponent dökme demir alaşımların faz denge diagramları, termodinamik ve termokimyasal özellikleri hesaplanmıştır.

High Si-Mo dökme demir içerisine aluminyum eklenmesi, ötektoidik faz geçiş sıcaklığını yüksek sıcaklıklara ötelemiştir. Faz geçişi sırasında meydana gelen anlık hacim değişimleri, çevrimsel yükler altında malzemeye zarar vermekte ve deformasyona uğratmaktadır. İşte bu yüzden egzoz manifold çalışma sıcaklıklarında faz geçişlerinin olması istenmez ve çalışma sıcalık aralığını belirleyen ana faktör budur.

Termodinamik hesaplamaların yanısıra; yapılan yüksek sıcaklık oksidasyon testleri göstermiştir ki, malzemenin oksidasyon direnci aluminyum miktarıyla doğru orantılıdır. Yüksek sıcaklık oksidasyon testleri farklı sıcaklıklarda ve yüzden fazla numune üzerinde gerçekleştirilmiştir. Tüm testler tekrarlanabilir özelliğe sahiptir. Oksit film karakterizasyonu ve yüzey üzerinde oluşan oksit fazlarının karaterizasyonu XRD, GDOES ve SEM ile yapılmıştır. Ayrıca $850^{o}C$ sıcaklık altında termal yorulma testi yapılmış. Termal yorulam testleri ısıtma soğutma olacak şekilde çevrimsel olarak gerçekleştirilmiştir. Yüzey üzerinde oksit çatlağı tespit edilene kadar test devam ettirilmiştir. Sonuç olarak aluminyum alaşımlı AlSiMo dökme demirlerin termal yorulma dirençleri tespit edilmiştir. Yüksek Si-Mo içerikli dökme demirlere göre iki kat daha iyi olduğu gözlenmiştir. Buna ek olarak elektro-kimyasal korozyon testi aluminyum alaşımlı yüksek silisyum ve molibdenli dökme demirler için yapılmıştır. Yirmidört saat süren bu test, tuz püskürtme şekliden $35^{o}C$ sıcaklık altında yapılmıştır.

Gözle görülür bir şekilde, aluminyum katksının elektro-kimyasal korozyon direncini arttırdı ispatlanmıştır.

Sonuç olarak, AlSiMo alaşımlı dökme demirler, aluminyumun yüzey üzerinde seçici difüzyon ve oksidasyonundan kaynaklı, malzemenin yüksek sıcaklık oksidasyon direncini arttırmaktadır. Yüzey üzerinde oluşan ince oksit filmi termal yüklemelere karşı dayanıklıdır ve aynı zamanda metal içine oksijen difüzyonunu engellemektedir. Yapı içeresindeki aluminyum katı eriyik sertleşmesine sebep olduğu için, malzemenin mekanik özelliklerinde de artış görülmektedir. Termodinamik hesaplamalar ve yapılan deneyler bir biriyle uyumludur.

1. INTRODUCTION

The exhaust manifold collects the exhaust gas from the cylinder head and throws out it through the exhaust pipe [1]. It is exposed to hot and corrosive exhaust gases combined with both thermal - and strain cycling during engine operation. It is shown in a schematic heavy-duty diesel engines exhaust-turbo manifold in the Figure 1.1. This kind of manifold consists of three subparts and middle part called as a turbo manifold, which is a double-channel compound and it is subjected to highest loads due to the boosted mass flow of exhaust gases and also to the additional load from the weight of the turbo charger.

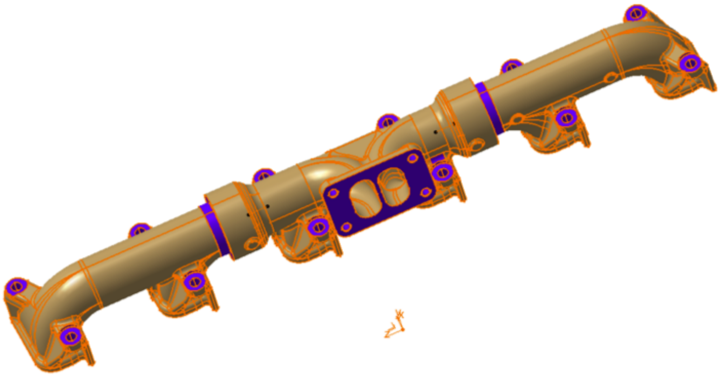

Figure 1.1: Schematic description of the hot end exhaust system of a six-cylinder Ford Otosan Eqotorq 9L diesel engine, showing the exhaust manifolds connected to a turbo manifolds.

Thermal stresses of exhaust manifolds have increased significantly in the last two decades. Nowadays, to raise the engine performance and overall efficiency is the most encountered challenge for the automotive industry, and at the same times, customer's expectation for safety, fuel economy and price would be fulfilled. Increasing efficiency and the new demands regarding the emissions causes the exhaust gas temperatures to increase [2]. All the state factors are taken into consideration, it is obviously seen that exhaust manifolds are operating very high thermal and mechanical stresses and requires new design approaches and material selections.

There are several demands on the exhaust system and they can be listed as follows;

- The backpressure in the exhaust system should be kept minimum.
- Acoustics need to be optimized.
- Durability and life must be high concerning thermal loads/vibrational loads/corrosion.
- Cost must be minimized.
- Emission standards should be fulfilled.

1.1 Purpose of Thesis

Considering all these demands on hot end exhaust systems, it is aimed that while increasing the high temperature oxidation, creep and fatigue resistance, it is intended to improve engine performance, reduce weight, and also increase the cost efficiency. In this case, we need to investigate;

- How to minimize thermal stresses
- How to minimize thermal deformations

During the study, we focus on improvement of High Si-Mo Ductile Iron by adding Aluminum for increased high temperature oxidation and thermal fatigue life in exhaust gas temperatures up to $1000^{o}C$. Additionally, this study includes computational thermodynamic calculations for the investigation of thermochemical and thermodynamics properties of Al-Si-Mo Cast Alloys and their high temperature oxidation behavior.

1.2 Failure Modes of Exhaust Manifolds

There are three main failure mechanism of exhaust manifolds. These are

- Thermo-mechanical fatigue,
- High cycle fatigue,
- Gasket leakage due to the cyclic plasticity.

In the aspect of thermo-mechanical fatigue, main factor is thermal loads, which are extreme temperature amplitudes and gradients, that cause the crashes of exhaust manifolds.

If the deformation in elastic region and applied stress level is relatively low, high cycle fatigue damage occurs. Vibrational loading due to the weight of turbocharger and close coupled catalyst, causes high cycle fatigue damage [3]. This kind of failure mode is not frequently observed.

The most encountered failures are manifold cracking caused by thermo-mechanical loading and exhaust gas leakage.All of them are connected to the materials selection, product design and boundary conditions. Next subsections, failure mechanism and sub-failure modes will be explained and discussed.

1.2.1 Thermo-Mechanical Fatigue

Integrated thermal and mechanical loading lead to ThermoMechanical Fatigue(TMF). In this context, stresses and temperatures depend on time. This type of loading can be more detrimental compared to isothermal fatigue at the maximum service temperature. Material properties, mechanical strain range, strain rate, temperature, and the phasing between temperature and mechanical strain all play a vital role in the thermo-mechanical fatigue failure formed in the material [4]. Thermo-mechanical loading is very often attained in start - stop cycles of high temperature components such as exhaust manifolds, engine cylinder heads, etc.

When comparing between isothermal and thermo-mechanical fatigue, it is the major difference is constraint. When increasing temperature, materials tend to expand. This expansion creates a tensile strength and it is often constrained by the surrounding cooler material. In that way, thermal strain is transformed into mechanical strain due to the fatigue damage in the material. If all the thermal stain is converted into mechanical strain, it can be claimed that total constraint occurs. Ratio of the thermal and mechanical strain rates give us measure of the degree of constraint.

Thermo-mechanical loading is frequently defined to be in-phase (IP) or out of phase (OP). A schematic view of TMF loading pattern under these two loading is given in Figure 1.2 [5]. In IP loading, the maximum temperature and strain happen at the

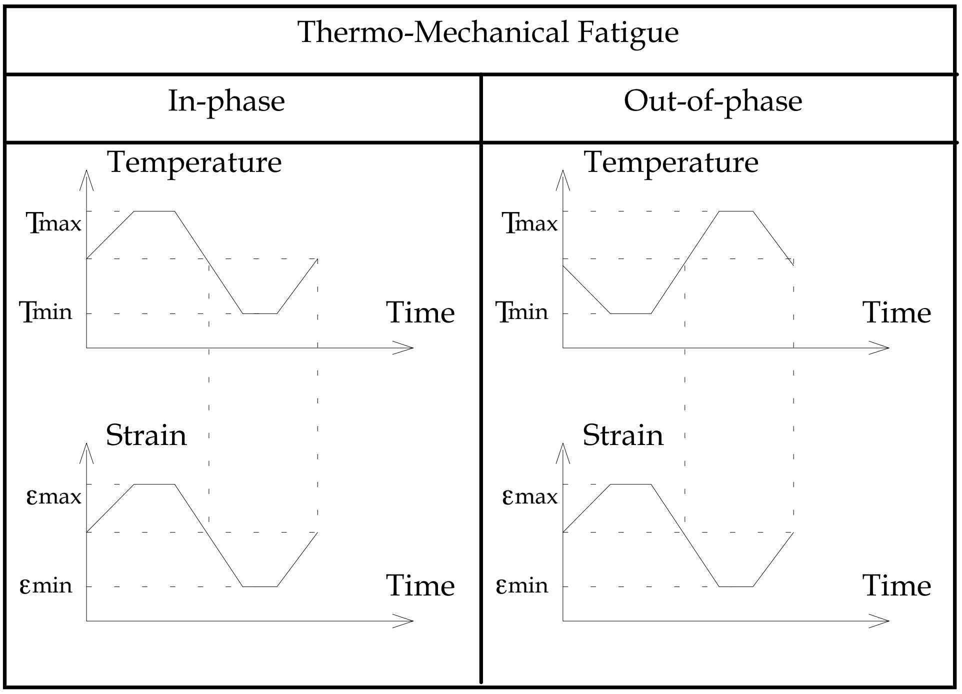

Figure 1.2: In-phase and out of phase TMF loading pattern.

same time. In OP loading, the material undergoes tension at lower temperatures and compression at highest temperature. Oxidation damage can be probably caused by OP loading because oxide film can form in compression strength at the higher temperature and then rupture during the following low temperature since the oxide film is more brittle under the tensile strength caused by the OP loading [4].

The total fatigue damage per cycle is defined by summing the damage due to mechanical fatigue, creep and oxidation, respectively. It is described in Equation 1.1 & 1.2 [6] [4]:

$$D^{tot} = D^{fat} + D^{ox} + D^{creep} \tag{1.1}$$

in terms of fatigue cycles,

$$\frac{1}{N^{tot}} = \frac{1}{N^{fat}} + \frac{1}{N^{ox}} + \frac{1}{N^{creep}} \tag{1.2}$$

1.2.1.1 Creep Mechanism

Basically, creep is a diffusion process. At high stresses, creep is controlled by the movement of dislocations. It is an example of self diffusion process. Dislocation creep has a strong dependence on the applied stress and no grain size dependence. At lower

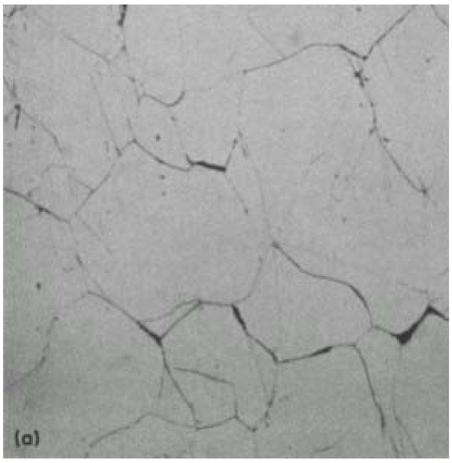

Figure 1.3: Creep damage in Type 316 stainless steel.

stresses, diffusion exists along the grain boundaries. It is shown in Figure 1.3 [6] that a triple point crack formed at the intersection of grains. As a result of grain boundary sliding, these microcracks shown in Figure 1.3 [6] form along the elongated grains. Creep is highly temperature and time dependent. Unlike the dislocation creep, grain boundary diffusion(Coble creep) to have a stronger grain size dependence.

The creep damage formulation shown in above Equations 1.3 & 1.4 is described by literature [4]:

$$\frac{1}{N_{creep}} = \int_0^{t_c} A_{cr}\Phi^{cr} \exp\left(\frac{-\Delta H^{cr}}{RT}\right)\left(\frac{\alpha_1\bar{\sigma} + \alpha_2\sigma_h}{K}\right)^m \mathrm{d}t \tag{1.3}$$

where $\bar{\sigma}$ is equivalent stress, σ_H the hydrostatic stress and K the drag stress. α_1 stress state constant and α_2 hydrostatic stress sensitivity constant. Φ^{cr} is the Creep Phasing Factor and it is described in following Equation 1.4.

$$\Phi_{ox} = \frac{1}{t_c}\int_0^{t_c} \exp\left[-\frac{1}{2}\frac{\left(\dot{\varepsilon_{th}}/\dot{\varepsilon_{mech}} - 1\right)^2}{\xi^{creep}}\right] \mathrm{d}t \tag{1.4}$$

where ξ^{creep} defines the sensitivity of the phasing to the creep damage. It is commonly supposed that creep damage occurs under the IP loading [7].

1.2.1.2 Oxidation Mechanism

The oxidation damage is caused by periodic formation of an oxide layer at the crack tip and its rapture [7]. In OP loading, when the material is hot and in compression load, an oxide layer can grow on the surface of material. The cross-section view of

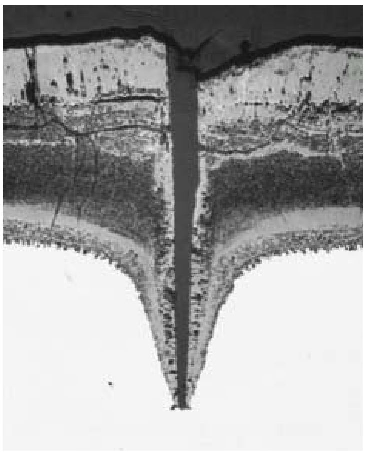

Figure 1.4: Oxidation Damage in Steel.

oxidation damage is seen in Figure 1.4 [6]. The oxide layer comes to be brittle at the lower temperature. Under the mechanical strain, the oxide film cracks and new clean metal surfaces emerge. This clean metal surfaces will quickly oxidize and the process duplicates itself during the new mechanical strain cycle. In the end, this cyclic process will create a crack, and it can be grown under the cyclic loading.

Oxide cracks can also form on the surface during IP loading. In that situation, during the heat up cycle, the oxide films grow on the surface, while the material is in tension. After the rapidly cooling, the oxide film expose a buckling moment and the fracture of oxide scale occurs. Oxidation damage is not a dominant under the isothermal loading conditions and rupture is not observed. Oxide film forms easier and faster at higher temperatures.

According to the study of Neu and Sehitoglu [4], oxide damage will happen when the strain range greater than a threshold for oxide cracking. Equation 1.5, 1.6, and 1.7 describe the oxidation damage and total cycles to failure due to oxidation.

$$if \Delta\varepsilon_{mech} > \varepsilon_0 \qquad \frac{1}{N^{oxidation}} = \left[\frac{H_{cr}}{\Phi_{ox} K_{peff}}\right]^{-\frac{1}{\beta}} \frac{2(\Delta\varepsilon_{mech})^{\frac{2}{\beta}} + 1}{\dot{\varepsilon}^{1-\frac{b}{\beta}}} \tag{1.5}$$

ε_0 threshold strain for oxide cracking.

H_{cr} constant related to critical oxide thickness

β mechanical strain range exponent

b thermal strain rate sensitivity exponent

$$K_{peff} = \frac{1}{t_c}\int_0^{t_c} D_0 \exp\left(\frac{-Q}{RT(t)}\right) \mathrm{d}t \tag{1.6}$$

where D_0 is a constant, Q is activation energy for oxidation and R the universal gas constant.

$$\Phi_{ox} = \frac{1}{t_c}\int_0^{t_c} \exp\left[-\frac{1}{2}\frac{(\dot{\varepsilon_{th}}/\dot{\varepsilon_{mech}}+1)^2}{\xi^{ox}}\right] \mathrm{d}t \tag{1.7}$$

ξ^{ox} oxidation phasing constant for thermal and mechanical strains.

Oxidation damage depends on strain rate, strain range and temperature. Oxidation rate is determined by the effective parabolic oxidation constant in Equation 1.6.

1.2.1.3 Fatigue Mechanism

Fatigue damage is crack growth and crack growth propagation caused by the cyclic loading. In the Figure 1.5(a) & 1.5(b) [8], an example of thermal fatigue crack is shown due to higher plastic strains [8]. As can be shown in Figure 1.5(b), A lot of microcrack form on the surface. However, some of them are able to nucleate into the bulk.

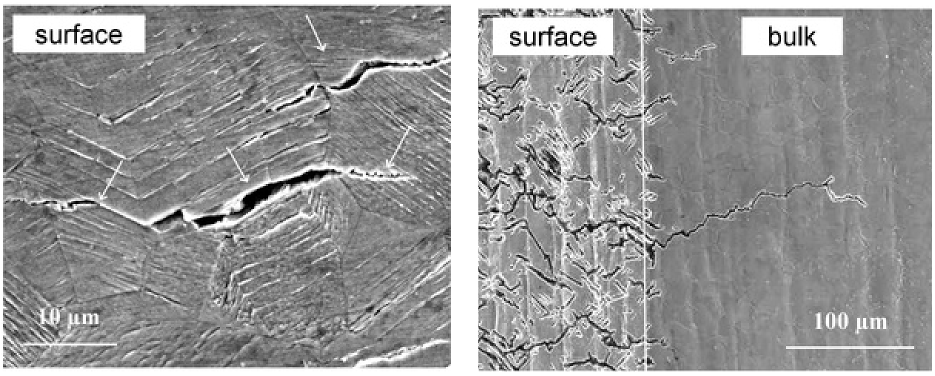

(a) SEM image of surface crack. (b) Cross section view of crack formation.

Figure 1.5: Formation of Surface Crack in Austenitic Steel.

Fatigue damage occurs at high strain ranges, strain rates and low temperatures [4]. Oxidation and creep effect are also negligible.

$$\frac{\Delta\varepsilon}{2} = \frac{\sigma_f'}{E}\left(2N^{fatigue}\right)^b + \varepsilon_f'\left(2N^{fatigue}\right)^c \tag{1.8}$$

where σ_f is the fatigue strength coefficient, E is the Young's modulus, b is the fatigue strength exponent, ε_f' is the fatigue durability coefficient, and c is the fatigue durability exponent. These constants above are determined from isothermal room temperature fatigue tests.

1.3 High Temperature Oxidation

High temperature oxidation plays an significant role in the selection of hot end exhaust system materials in especially automotive industry. As mentioned before, Oxide formation occurs easily and faster at high temperature. For this reason, most high temperature alloys are designed to react with the oxidizing environment in such a way that a protective oxide scale forms [9].

Oxide scale should behave a slow rate, strong adherence to the substrate, a high chemical stability and free of defects. Generally speaking, an alumina, chromia and silica scale can satisfy these requirements for high temperature oxidation resistance.

1.3.1 Thermodynamics Aspects

The metal initially absorbs oxygen and then chemical reaction ensues to form an oxide. Thus, the oxide first nucleates and then grows to form a scale on the metal surface. According to its oxidation kinetics, this oxide scale may protect the metal surface or not.

In General, oxide formation can be related by the reaction 1.9:

$$\frac{2x}{y}M + O_2 = \frac{2}{y}M_xO_y \tag{1.9}$$

where M_xO_y is the product of metal M and oxygen O_2. Under equilibrium conditions, the equilibrium constant of reaction 1.9 can be written as follow:

$$K_1 = \frac{a_{M_xO_y}^{\frac{2}{y}}}{a_M^{\frac{2x}{y}} P_{O_2}} \tag{1.10}$$

where K_1 is the temperature-dependent equilibrium constant, a_i is the activity of species i, and P_{O_2} is the partial pressure of oxygen. The oxidant gas,which is oxygen in this context, can behave as an ideal at relatively high temperatures, so the activity of oxygen can be estimated by its partial pressure in atmosphere.

The reaction occurs spontaneously, if the overall Gibbs free energy changeΔG is negative. The Gibbs free energy change is written as:

$$\Delta G = \Delta G^o + RT\ln(K_1) \tag{1.11}$$

where ΔG^o is the standard Gibbs free energy, T is temperature, R is the gas constant. If $\Delta G = 0$, the system is at equilibrium, the Equation 1.11 becomes as

$$\Delta G^o = -RT\ln(K_1) \tag{1.12}$$

Equation 1.10 and 1.11 determine the minimum oxygen partial pressure to form the oxide scale. If the dissociation partial pressure is less than the ambient partial pressure of oxygen, the oxide scale can be formed on the surface.

In order to estimate whether the reaction takes place under given conditions, the Elingham Diagram, which summarize the temperature dependence of standard Gibbs free energy for various common oxidation reactions at $P_{O_2} = 1atm$ can be used [10].

It is demonstrated in the Ellingham Diagram shown in Figure 1.6 [11] that the lower lines, which has more negative the standard free energy, indicate to form more stable oxide scale. In other words, Elements with higher oxygen affinity has relatively low the standard Gibbs free energy to form the oxide scale. For example Al_2O_3 and SiO_2 are more stable than FeO, NiO because their lines lower in Figure 1.6.

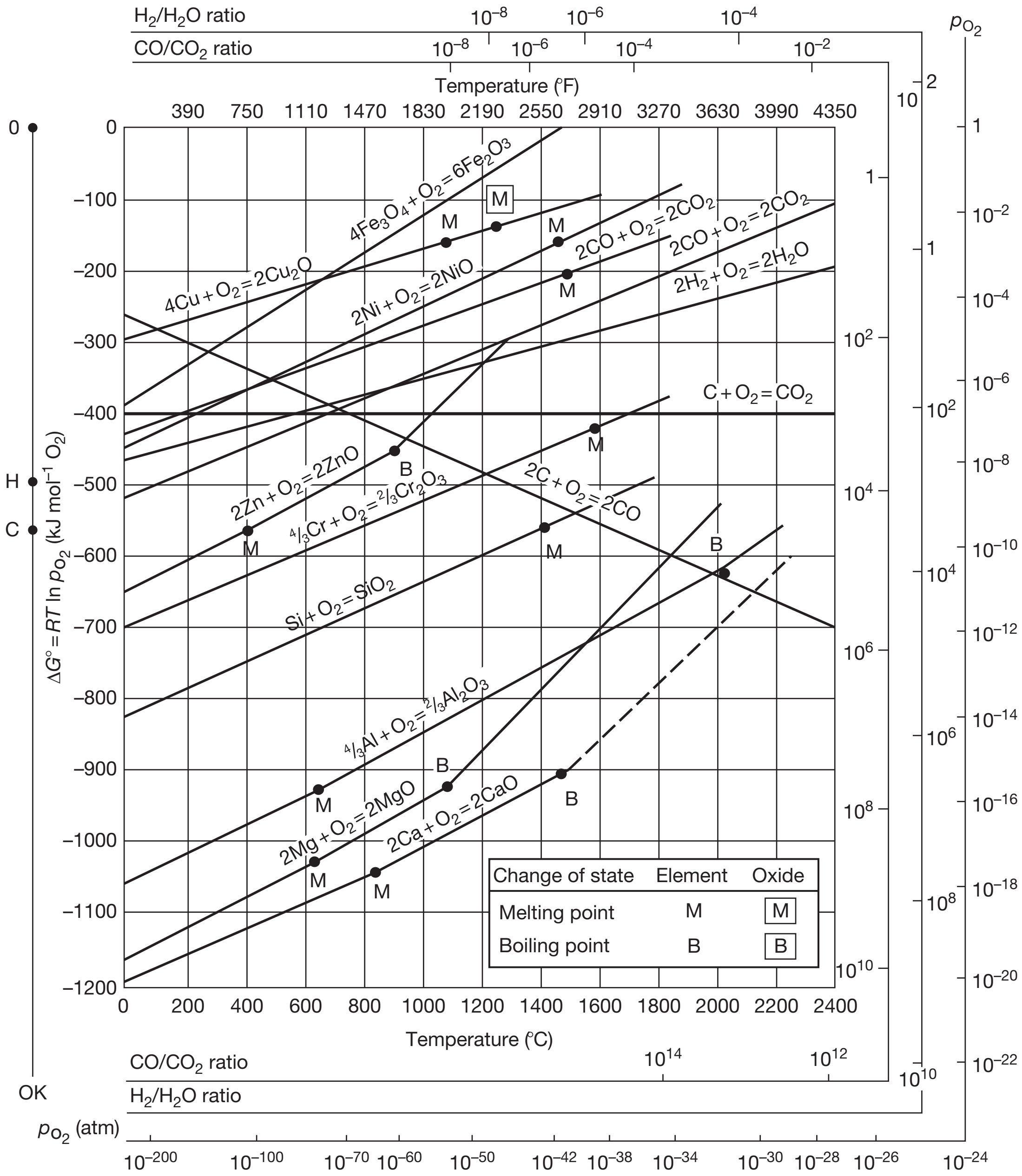

Figure 1.6: The Ellingham Diagram.

1.3.2 Kinetics of Oxide Formation

It is shown in Figure 1.7 [12] that the rate of oxide formation divided into three groups. These are linear rate law, logarithmic rate low and parabolic rate law. The general law can be written as :

$$x^n = kt + C \tag{1.13}$$

where x is the thickness of the oxide, k is rate constant, t is the oxidation time, C is the integration constant, and n is the power exponent.

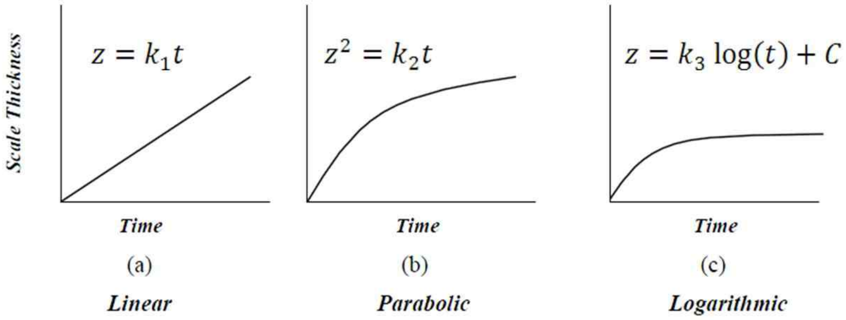

Figure 1.7: Schematic description of various oxidation type.

When n equals 1, it is stated that the linear rate law is used. Phase boundary reaction controls the kinetics rather than a transport process due to the results of linear rate law. Linear kinetics is also possible if the oxide is volatile or molten, if the scale spalls or cracks, or if a porous, non-protective oxide forms on the metal [11].

Second, the logarithmic rate law is used at low temperatures (i.e., $T < 300 - 400^oC$), and oxidation rates are often inversely proportional to time.

$$\frac{\mathrm{d}x}{\mathrm{d}t} = \frac{k}{t} \tag{1.14}$$

When integrate to both of sides, oxide thickness can be written in this form,

$$x = k_a \log(k_b t + 1) \tag{1.15}$$

where k_a and k_b are constants. Logarithmic oxidation rate law is usually employed for relatively thin oxide scales at low temperatures [10].

Third, when n equals 2, the oxide growth mechanism is expressed to the parabolic rate law. In the high temperature growth, the oxidation rate is controlled by diffusion through the scale [13] and the classic Wagner's theory assumes parabolic kinetics.

When integrate to Equation 1.14, then it forms as,

$$x^2 = 2k'_p t + C \tag{1.16}$$

where $k_p = 2k'_p$ is parabolic rate constant.

In high temperature oxidation kinetics, the parabolic rate law is always used. The relatively thick scale due to the diffusion dominates reaction rates. Growth of the diffusion controlled oxide scale is thermally activated. According to the Arrhenius equation, the rate increases exponentially with temperature as given in Equation 1.17

$$k_p = k_o \exp\left(\frac{-Q}{RT}\right) \tag{1.17}$$

where k_o is a constant, and Q is the activation energy for oxide-scale growth.

On the other hand, according to Wagner's Theory, Assumptions about oxide formation are listed as follows:

- The formed oxide scale is dense, well adhered to a metal surface and non-porous.
- Oxygen has only limited solubility in the metal.
- There are no space charge effects across the oxide and at the metal/oxide and oxide/gas interface.
- At each place in the scale as well as at the interfaces, local thermodynamic equilibrium is established.

As pointed out in Figure 1.8 [14], the oxide formation includes fluxes of both ionic and electronic charged species. The driving forces for these fluxes are connected to the chemical potential gradient and electrostatic field. The relative migration rates of cations, anions, electrons, and electron holes must also be balanced such that no net charge build up occurs within the scale [10].

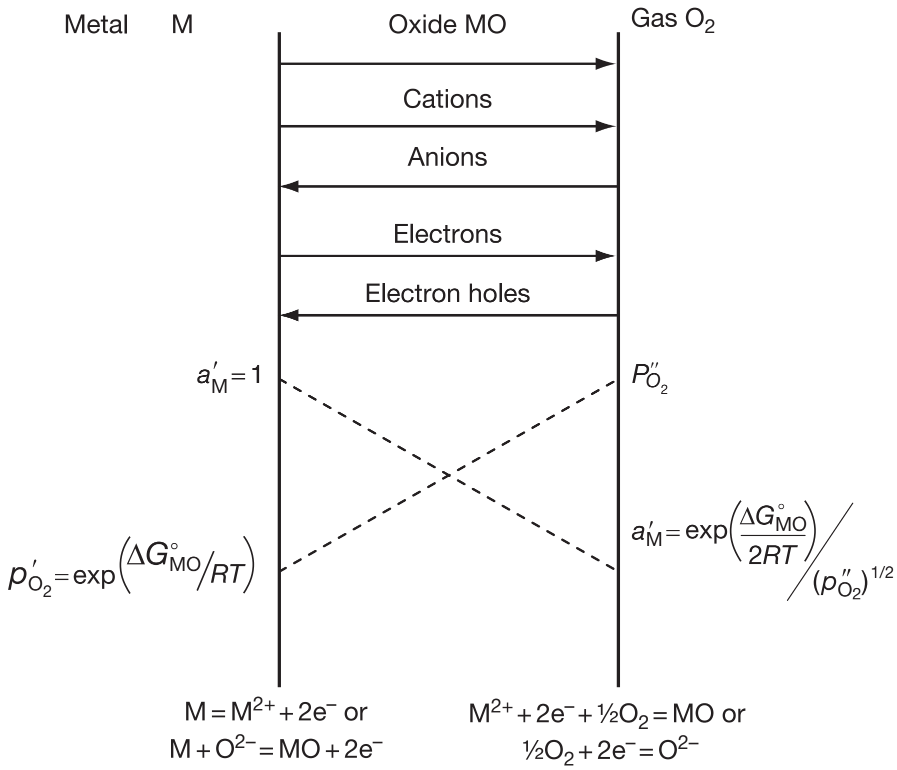

Figure 1.8: Schematic illustration of Wagner's theory for transport process.

1.4 Materials

Hot end exhaust systems such as exhaust manifolds are the hottest part of the engine. Materials selection is a big challenging due to the higher demands from exhaust manifolds but the main desired property is always heat resistance. For this reason, ferritic or austenitic ductile cast irons and as well as cast stainless steel are preferred by automotive companies. According to the literature review, it is demonstrated that there is a relationship between exhaust manifold service temperature and used materials. It is shown in Figure 1.9 [15].

According to Figure 1.9, it is shown that there are several cast alloys to used as exhaust manifold materials but nowadays, four of them commonly used in diesel and gasoline engines. These are ferritic ductile iron, which is called High Si ductile iron, High Si-Mo ductile or compacted graphite iron, austenitic ductile iron and ferritic or austenitic stainless steel.

- Gray Iron **(1)**
- Compacted Graphite Iron **(2)**
- Ductile Iron (D4512) **(3)**
- Hi Silicon ductile Iron **(4)**
- Hi Silicon -Molybdenum Ductile Iron **(5)**
- Austenitic Ductile Iron (D5S) **(6)**
- Fabricated Stainless Steel **(7)**
- Cast Stainless Steel **(8)**

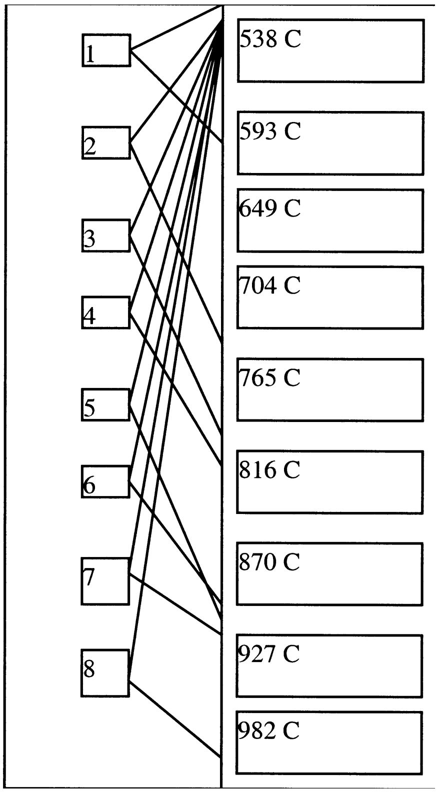

Figure 1.9: Temperature limits of various exhaust manifold alloys.

Thermo-physical and thermo-mechanical properties increase from ferritic ductile iron to stainless steel but machining of product, castability of alloys get harder, and also cast efficiency decreases.

Materials relative selection preferences are given in Figure 1.10 [15].

	Austenitic	**Ferritic**
Cost		Preferred
Coefficient of Thermal Expansion		Preferred
Thermal Conductivity	Preferred	
Elevated Temperature Strength	Preferred	
Oxidation Resistance		Preferred
Fracture Toughness	Preferred	
Weldability	Preferred	
Formability	Preferred	
Hot Salt Corrosion		Preferred

Figure 1.10: Relative Selection Preferences.

Moreover, there are generally three types of cast irons according to their graphite shape, which is seen in Figure 1.11. These are grey irons, compacted graphite irons and ductile irons.

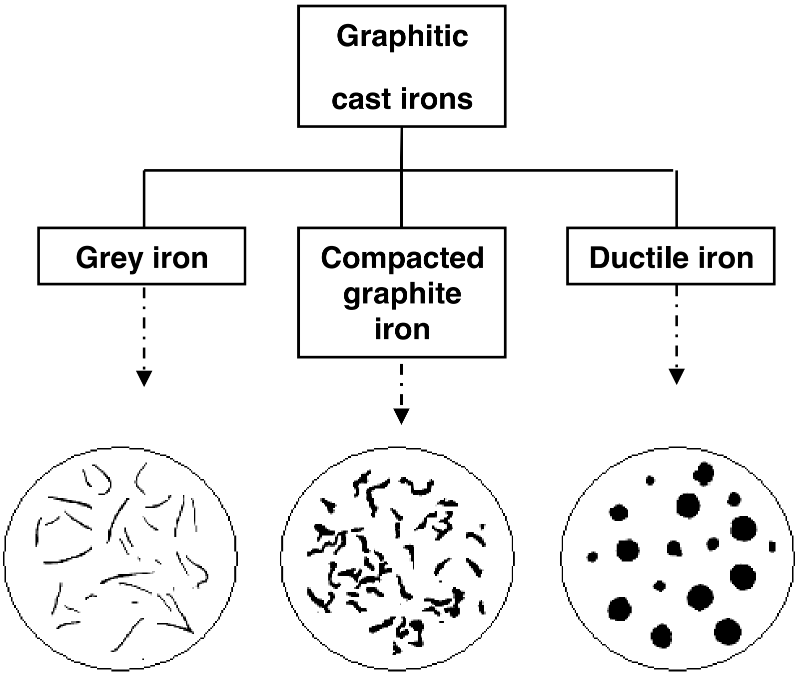

Figure 1.11: Types of cast irons according to their graphite morphology.

As shown in Figure 1.11, the graphite phase in grey cast iron appears as individual flake shape. Flake graphites are elongated and randomly oriented. Usual microstructure of gray iron is a matrix of pearlite with graphite flakes dispersed throughout. Generally it contains 3 - 4 wt% carbon. Cooling rate affects the microstructure dominantly. It is always desired to have very slow cooling rate in the automobile industry application. Very slow cooling of irons that contain large percentages of silicon and carbon is likely to produce considerable ferrite and pearlite throughout the matrix, together with coarse graphite flakes [16].

The most important weakness of grey cast irons is their lack of toughness associated with the brittleness and morphology of the graphite flakes, which promote the initiation and propagation of microcracks [17].

Second type of cast iron is compacted graphite iron, which is also called vermicular graphite, upgraded or semiductile cast iron. The graphite morphology is relatively complex compared to grey and ductile irons. Compacted graphites appear as spheroidal and vermicular particles. Vermicular graphites are shorter and thicker, and have rounded edges to compared with flake graphite. They are interconnected within the eutectic cell. These interconnected graphites supplies better thermal conductivity. As mentioned before, compacted graphite iron consists some spheroidal graphite particles. These number of nodular graphites determine such properties as castability, machinability and thermal conductivity.

Ductile cast iron is schematically shown in Figure 1.11. Spheroidal graphite morphology is obtained by means of a special liquid metal treatment. As in gray cast iron, cooling rate affects the graphite morphology. For homogeneous nodular graphite morphology, very slow cooling rate is necessary. Ductile cast iron is much stronger and has higher tensile elongation than gray irons. Ductile iron can be alloyed with larger amount of silicon, chromium, nickel or copper to improve high temperature oxidation, corrosion and abrasion properties.

1.4.1 High Si-Mo Ductile Iron

The current maximum temperature of diesel exhaust gases in heavy-duty diesel engines is approximately 750^oC. Up to this temperature, the most widely used material is High Si-Mo Ductile Iron. High Si-Mo consist of ferritic iron matrix, spheroidal graphite and M_6C participates along the grain boundaries. High silicon and molybdenum content are added to matrix for improving corrosion resistance, mechanical strength at high temperatures, respectively. Chemical composition of High Si-Mo is given wt % in Table 1.1.

Table 1.1: Chemical Composition of High Si-Mo Alloys.

Alloy	C	Si	Mn	Cr	Ni	Mo	Mg
High-SiMo	3.17	4.15	0.4	0.1	0.04	0.86	0.04

1.4.2 Austenitic Ductile Iron

When the exhaust-gas temperature is increased, this alloy shows limitations as mentioned before. Therefore, many manufacturers change the materials despite of expensive,which is named austenitic ductile iron(Ni-resist D5S), commonly used in gasoline engines' exhaust manifolds. Due to the its microstructure, it has higher strength at high temperature but the oxidation resistance is relatively lower than the High Si-Mo. According to ASTM A439 standard, D5S which is commonly used in exhaust manifolds containing 34-37 wt % Ni, 4.90 - 5.50 wt % Si and 1.75 - 2.20 wt % Cr.

1.4.3 Stainless Steel

Final material group used in exhaust manifolds is cast stainless steel. Both ferritic and austenitic cast stainless steels are used due to the high cost of austenitic ductile iron. It is known that these alloys show high strength and corrosion resistance at high temperatures due to the fact that they consist of high Ni and Cr content. However, stainless steel shows poor castability due to its low carbon content and consequences of higher melting temperatures. Low carbon content can also affect to the microstructure, negatively. It contains large grains and for this reason, ductility and fatigue life decrease. Consequently, ferritic steel are used to exhaust manifolds made of sheet metal obtaining grain size reduction by metal forming [18].

On the other hand, The end point of this work is austenitic cast stainless steel. They are generally used in high-power gasoline engines under 1000^oC exhaust gas temperature.

2. THERMODYNAMIC ASSESSMENTS

2.1 Introduction

New and demanding applications assemble to development of new materials are critical for persistent improvements in the quality of human life. Conventionally, Materials science and engineering has mostly focused on structure property relations, measuring material properties and, processing materials. This practical approach is to change toward the design of materials for optimal functionality, driven by advances in computational materials science in the last few decades [19].

Phase diagrams have mainly been the domains of a limited number of specialists because of the complications many scientists and engineers have in understanding them, especially at the ternary and higher-order level [20].

Since phase diagrams are generally used to point out only binary and ternary alloys, their use has also been seen as rather academic, as almost all real materials are multi-component in nature. The CALPHAD method has changed this perspective as it is now feasible to calculate the phase behavior of highly complex, multicomponent materials based on the extrapolation of higher-order properties from their lower-order binary and ternary systems [21]. In addition, the method can be joined with kinetic formalisms so that we could recognize and predict how materials act in conditions away from equilibrium, which enhances its value.

There are many applications of theoretical thermodynamic models, as these are the basis of the CALPHAD method. Nothing would be possible without the existence of the computational methods and software, which allow these models to be applied in practice [20]. In principle, subjects involved in computational methods are less different and mainly revolve around Gibbs energy minimization [22]. Optimizer codes are used by the computational methods. The prior purpose of these optimizer codes, which is used for the thermodynamic assessment of phase equilibria, is to reduce the statistical error between calculated phase equilibria, thermodynamic properties and the equivalent experimental values [20].

To sum up, Calphad approach makes easier to understand and calculate true thermodynamics equilibria properly. It makes connection between theory and experiments. As can be stated in the above, all real materials are multi component in the nature and it is not easiest to assess phase diagrams and equilibria. Calphad Method allows us to calculate and predict accurately real world materials, which is used in engineering applications. Next section, Calphad approach is defined basically and discuss about on multi-component applications.

2.2 CALPHAD Aproach

Calculation of Phase Diagrams which is shortly named Calphad [20, 21], is an analytical representation of Gibbs free energy of each individual phases in a system in terms of state variables, temperature, pressure and composition etc. [22]. Gibbs derived the well known equilibrium condition that the chemical potential μ_n^φ of each component n is the same in all phases φ.

$$\mu_n^l = \mu^l l_n = \cdots = \mu_n^\varphi n = 1,2,3,\ldots \tag{2.1}$$

Gibbs energy of a system depends on the chemical potentials is defined in Equation 2.2.

$$G = \sum_{i=1}^{n} \mu_i x_i \tag{2.2}$$

These definition of the Gibbs energy can be used together with Equation 2.1 in numerical calculations to minimize the Gibbs energy for prescribed conditions. All of the Calphad type software tools use methods like the two-step method of Hillert [23] or the one step method Lukas et al. [24] to minimize the Gibbs energy. For unknown parameters the ideal values could be obtained by weighted nonlinear least squares minimization method and they could be solved numerically, for example using a Newton-Raphson technique. Schematic flowchart of the Calphad Method is presented in Figure 2.1. Thermodynamic calculations in this study were carried out by the Thermo-Calc software [25], using TCFE6 and SSUB4 database.

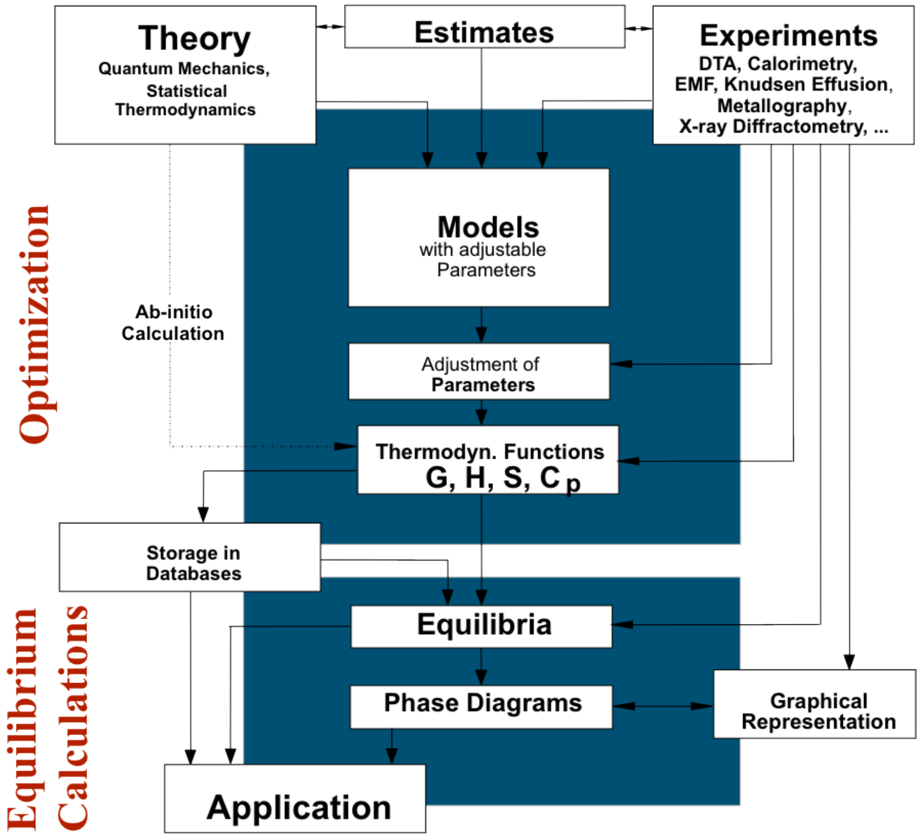

Figure 2.1: Schematic flowchart of the Calphad Method.

Molar Gibbs energy of a system is described in following Equation 2.3;

$$G(T) = a + bT + cT\ln(T) + \sum_n d_n T^n \qquad \textbf{(2.3)}$$

The coefficient a is related to the enthalpy, b is related to the entropy, c and d_n describe the temperature dependence of heat capacity. If we differentiate the Gibbs energy defined in Equation 2.3, thermodynamic functions, i.e. enthalpy, entropy and heat capacity, can be derived as follows;

$$H(T) - H^{SER} = a - cT - \sum_n (n-1) d_n T^n \qquad \textbf{(2.4)}$$

$$S(T) = -b - c - c\ln(T) - \sum_n n d_n T^{n-1} \qquad \textbf{(2.5)}$$

$$C_p(T) = -c - \sum_n n(n-1) d_n T^{(n-1)} \tag{2.6}$$

All of them equations are expressed as a power series of temperature and they are valid for temperatures above the Debye temperature [26]. In Equation 2.4, H^{SER} is the constant enthalpy values of Stable Element References at 298.15 K and 1 bar because the enthalpies cannot be defined absolutely [27].

Up to now, Calphad method and its theoretical background are explained. In the next two section, results of thermodynamic calculations will be presented.

2.3 Thermodynamic Properties of AlSiMo Alloys

Before the thermodynamic calculations of Fe-Si-Al-Mo-C system, state variables and constants are defined. While calculating the phase diagram of system, temperature and carbon content are selected as state variables. Pressure is set to 1 bar and system size is took 1 mole. According to these definitions, optimal aluminum, silicon, and carbon contents are obtained. Finally, Optimum chemical compositions of AlSiMo alloy are attained, after the systematic calculations and optimizations.

Calculated phase diagram of Fe-Al-Si-Mo-C multi-component system is shown in Figure 2.2

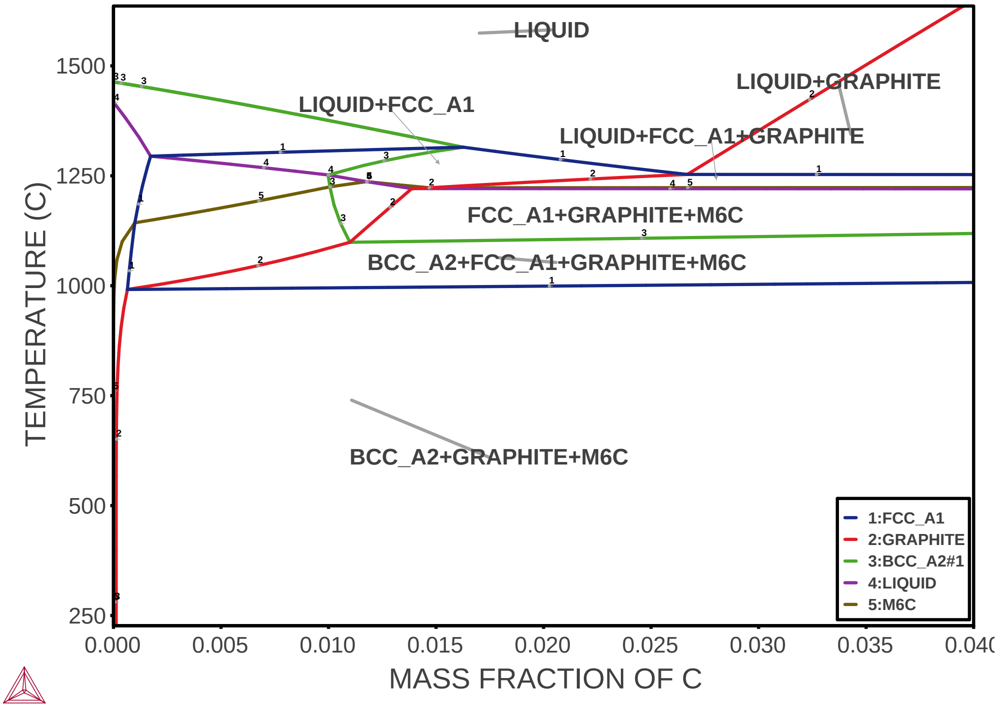

Figure 2.2: Calculated isopleth of Fe-Al-Si-Mo-C system, C section.

It can be considered as a modified Fe-C phase diagram for the AlSiMo Alloy. It is obviously seen that $\alpha - iron$, graphite and M_6C phases are stable under the exhaust manifolds' service temperatures. The most important thing that eutectoidic phase transition temperature(A1),which is first, blue, horizontal line shown in Figure 2.2, is shifted to higher temperature. It means that the service temperature of hot end exhaust systems is enlarged.

Another calculated isopleth is illustrated in Figure 2.3. The difference between Figure 2.2 and Figure 2.3 is that carbon composition is constant and composition of aluminum is varied between 0 to 9 wt%.

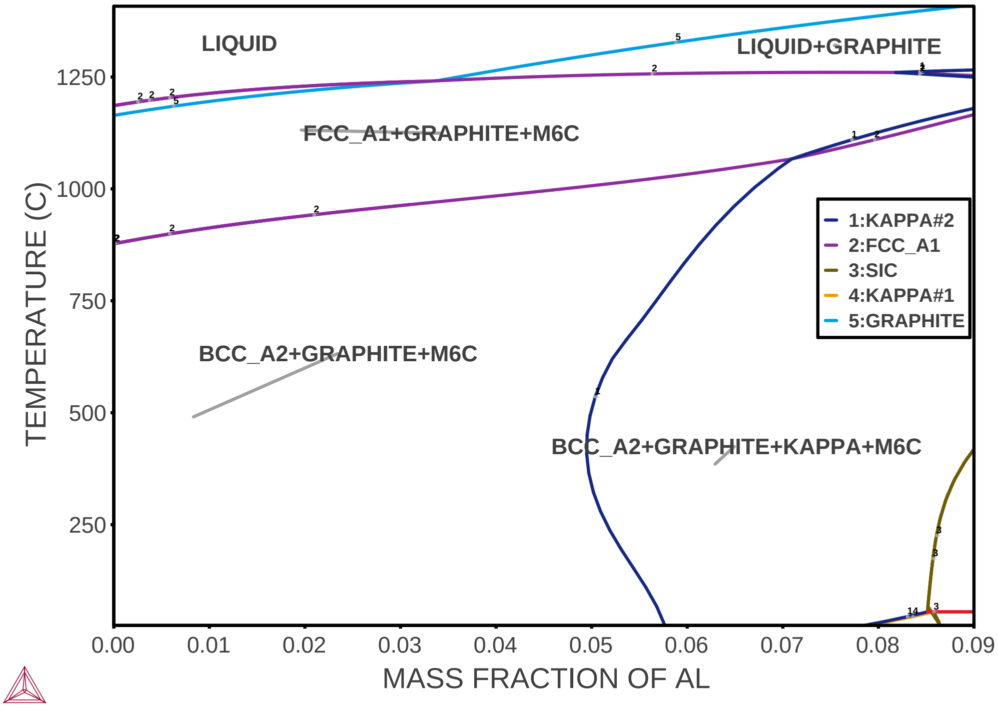

Figure 2.3: Calculated isopleth of Fe-Al-Si-Mo-C system, Al section.

According to Figure 2.3, it is encountered that there is an κ - carbide phase after the 5 wt% Al. An upward elbow shape line splits the stable phase region between room temperature to 1000^o C. The κ-carbide phase is FCC ordered phase and it fills interstitial sites in the structure [28]. This carbide phase increases the hardness locally but the structure could be brittle.

Results of these calculations gives us an optimal chemical composition of AlSiMo alloy to use in exhaust gas service temperatures. Chemical compositions are given in following Table 2.1

Table 2.1: Chemical Composition of AlSiMo Alloy.

Elements	Compositions (wt%)
Fe	Balanced
C	*** - ***
Al	*** - ***
Si	*** - ***
Mo	*** - ***
Mn	0.1 - 0.2 max.
P	<0.04
Cu	0.10 max.
Cr	0.10 max.
Ni	<0.1

As mentioned before, the eutectoidic phase transition temperature (A1) is shifted to higher temperature. In order to better understand, temperature dependent fraction of a component in all phases diagrams could be observed.

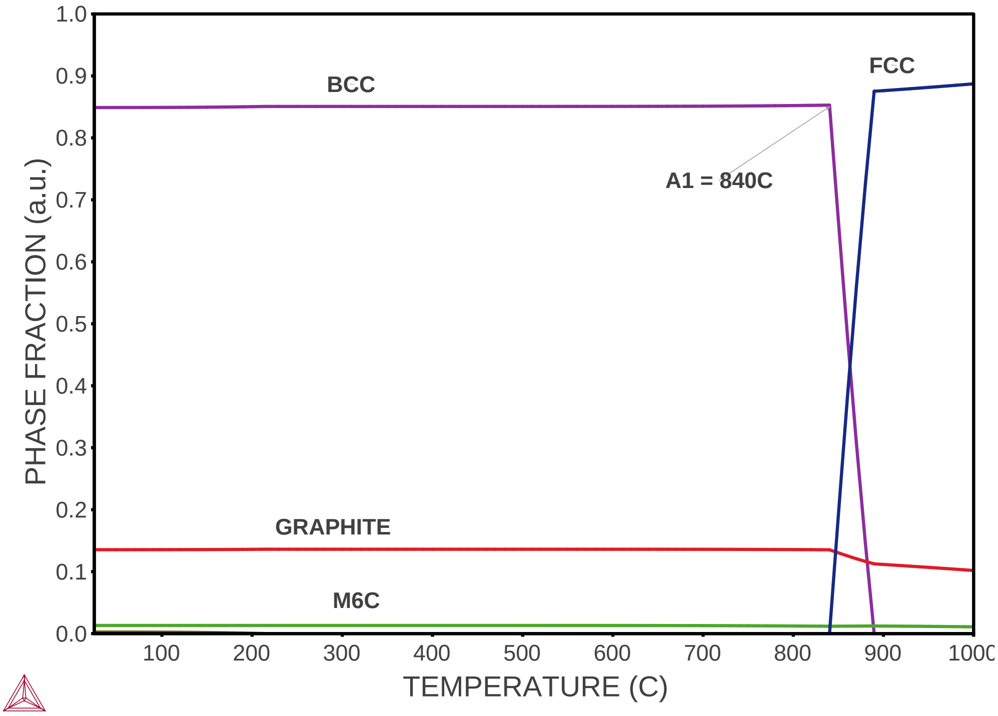

Figure 2.4: Temperature dependent phase fraction diagram of High Si-Mo Ductile Iron.

According to Figure 2.4 & 2.5, Colors indicate the stable phases in that composition, and it is clearly seen that A1 temperature shifted to 1000^oC with the addition of aluminum.

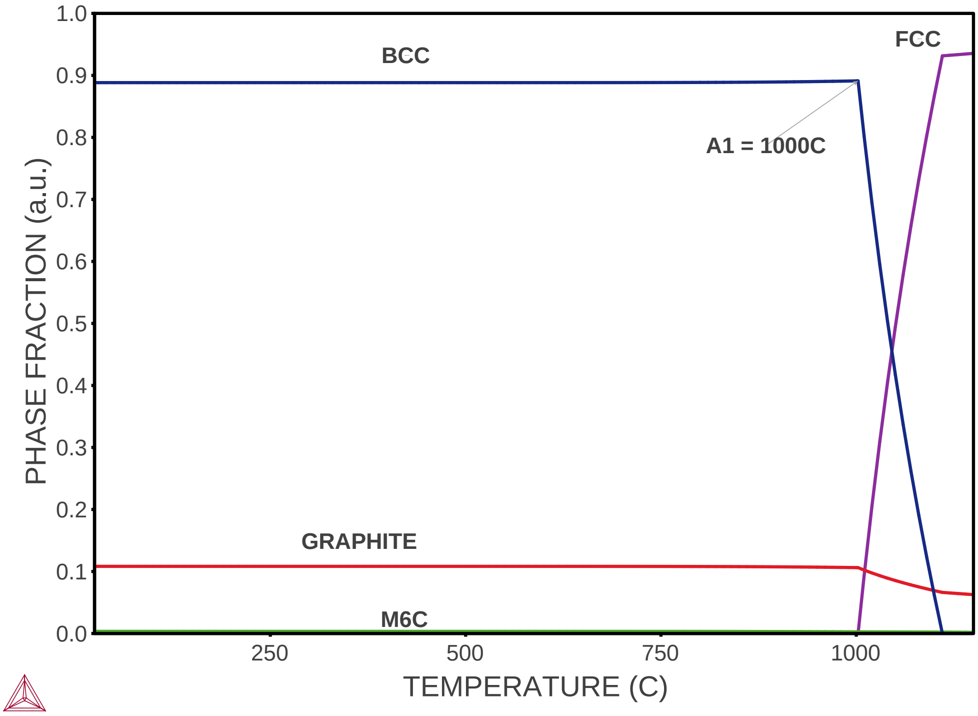

Figure 2.5: Temperature dependent phase fraction diagram of AlSiMo Alloy.

After that, another important results obtained from calculations are volumetric change due to the phase transition and temperature dependent heat capacity. With the increasing temperatures, the materials tends to expand. This expansion is directly related to the thermal expansion coefficient of materials, and molar volume change with temperature. In Figure 2.6, Molar volume is linearly increasing at the end of eutectoidic phase change temperature, and then it abruptly changes. This sharply decreasing is very detrimental under the cyclic thermal loads.

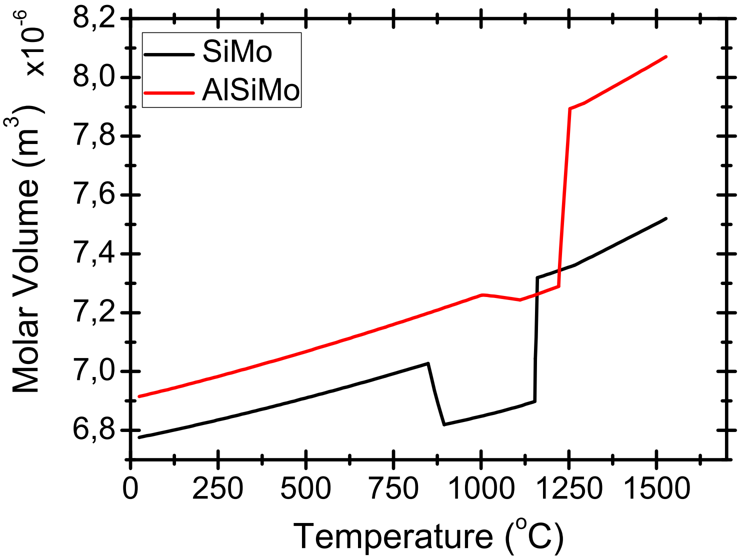

Figure 2.6: Temperature dependent volumetric change.

On the other hand, Aluminum containing High Si-Mo cast iron is linearly increasing similar to High Si-Mo. However, Molar volume change is decreasing slowly not abruptly, after the A1 temperature.

In Figure 2.7, thermal expansion coefficients are calculated in post-processing part. According to Lu X. et all study [29], Molar volume can be expressed as:

$$V_m = V_0 \exp\left(\int_{T_0}^{T} 3\alpha dT\right) \tag{2.7}$$

where V_0 is the molar volume at the reference temperature, T_0. α indicates the coefficient of linear thermal expansion. Volumetric expansion 2.8 is defined between room temperature and melting temperature in literature [29].

$$3\alpha = a + bT + cT^2 + dT^{-2} \tag{2.8}$$

Thermal expansion coefficients are assessed based on Equations 2.7 & 2.8. It is seen on the Figure 2.7 that thermal expansion of aluminum containing High Si-Mo cast iron is slightly shifted to upper values. However, this slightly change can be ignored. Generally speaking, it is admitted similar to High Si-Mo cast iron.

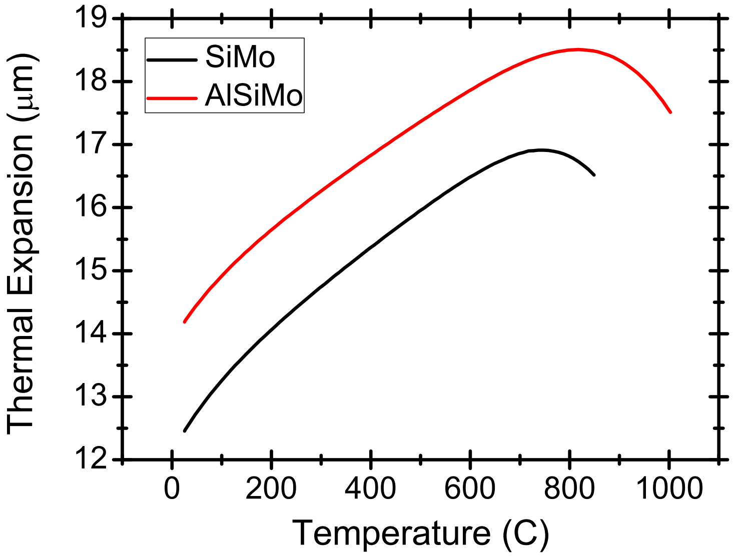

Figure 2.7: Calculated thermal expansion coefficient.

Finally, Temperature dependent heat capacities are calculated both of them and compared each other. Up to the magnetic phase transition temperature which is the peak temperature shown in Figure 2.8, heat capacity values are almost the same for all compositions. However, the addition of aluminum slightly decreases the heat capacity.

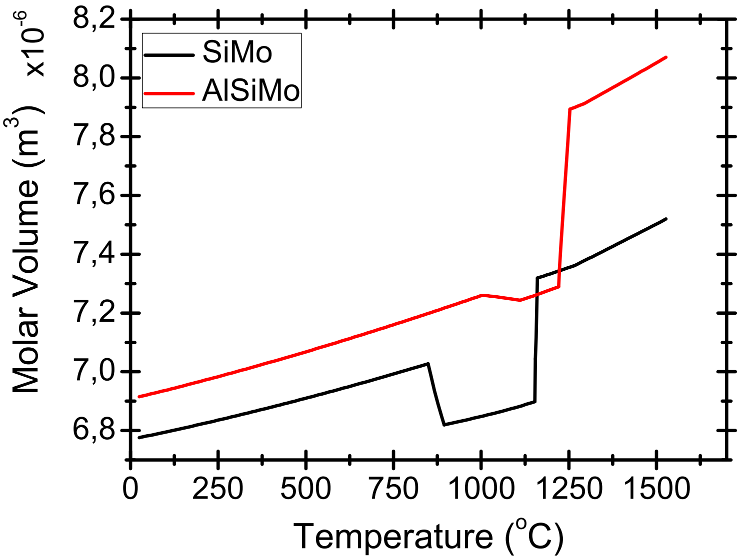

Figure 2.8: Temperature dependent heat capacity.

2.4 High Temperature Oxidation Model

In this section, High temperature oxidation behavior of AlSiMo alloys are presented. Oxidation model includes only thermodynamic assessments. Calculations are performed for 650^oC, 750^oC, 850^oC. Atmospheric conditions are taken as a reference state, so partial pressure of oxygen (P_{O_2}) is set to atmospheric condition.

According to the oxidation model at elevated temperatures, when all phases occurred on the substrate surface become stable, mass fraction of oxide phases change slightly. In the calculation of oxide scale structure, the TCFE6 and SSUB4 databases are used for the matrix and the oxides, respectively. Based on these calculations, Aluminum is believed to affect the oxide scale by forming a spinel, $FeAl_2O_4$ with Fe_2SiO_4 and the more protective Al_2O_3 and SiO_2 oxide at exposures in atmospheric condition at $650-850^oC$. Additionally, Al_2SiO_5 oxide phase more heat resistance than other iron-oxides and silicon-oxides.

The result of high temperature oxidation model for 850^oC is seen in below.

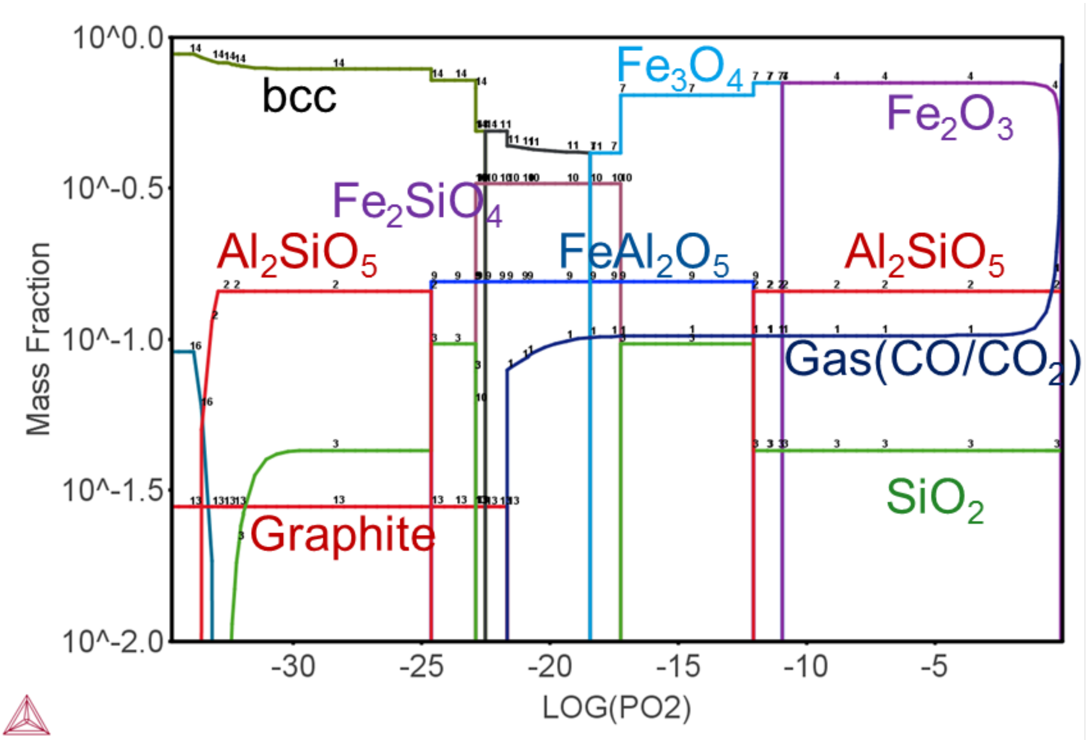

Figure 2.9: Calculated graph of mass fraction depends on partial pressure of oxygen.

In Figure 2.9, oxide phases formed on the bulk surface could be detected easily. Partial pressure of oxygen decreases to inner sides. If we schematically describe this graph, it can be drawn as in Figure 2.10.

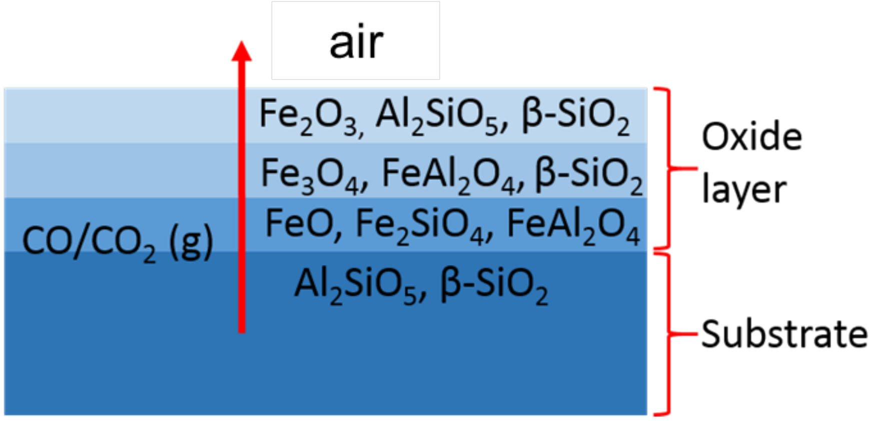

Figure 2.10: Cross-sectional view of oxide scale.

According to the calculation result, hematite, aluminasilicate, ironaluminate, fayalite and quartz phases are grown on the substrate surface. The arrow indicates flow of $CO-CO_2(g)$. Especially, aluminasilicate and ironaluminate make protective layer on the surface which block the diffusion of oxygen inside the bulk, and also these oxide phases increase the thermal resistance of materials.

3. EXPERIMENTAL STUDIES

In this chapter, it is aimed to show results and validations obtained from the thermodynamic assessments. Mostly, it is emphasized on high temperature oxidation and thermo-mechanic behavior of AlSiMo Alloys under the high thermal loads but first casting procedure, and sample preparation techniques are explained, respectively. After that TG /DTA measurements are discussed for detecting A1 temperature, and to compare with the calculation results. It is one of the significant outcome from the study. Another important outcome obtained from experimental studies are high temperature oxidation and thermal fatigue test at elevated temperature. These test results reveal how the material is resistant and durable against very high thermal loads. Finally, micro-hardness tests and accelerated corrosion test are discussed.

Flow chart of sample preparation and characterization are presented in Figure 3.1.

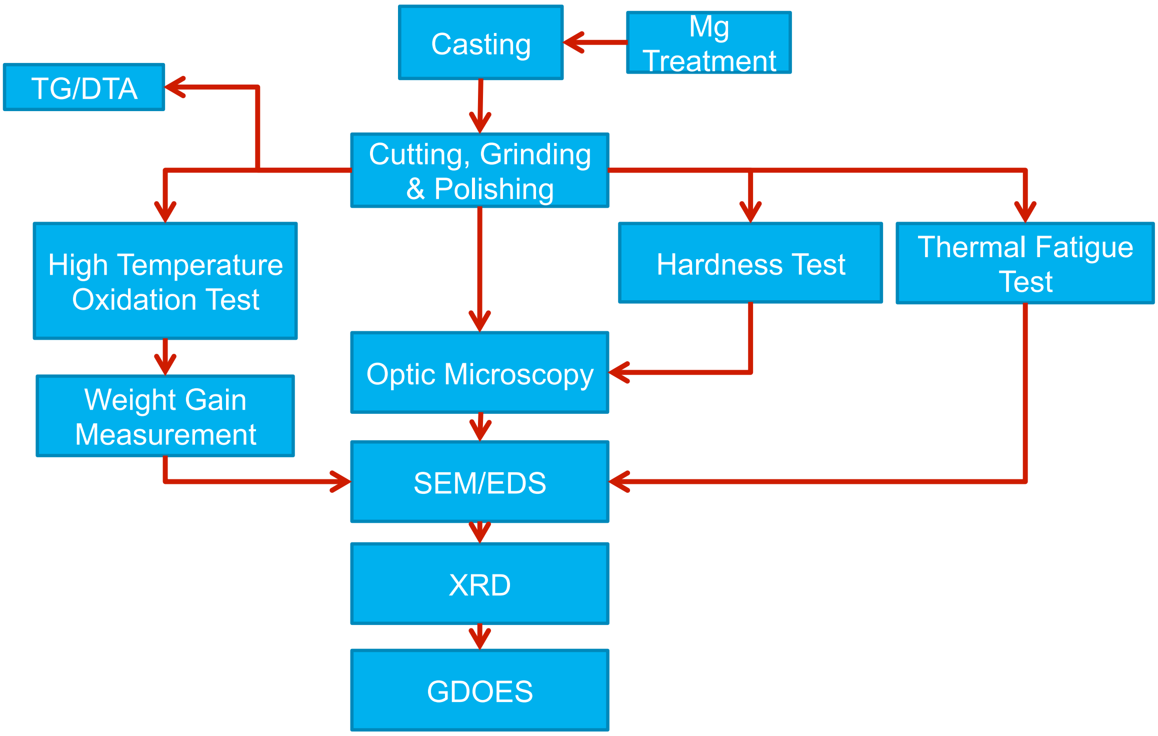

Figure 3.1: Flow Chart of Sample preparation & characterizations.

3.1 Casting

In addition to thermophysical, thermomechanical and thermochemical properties of materials, casting properties are also significant for serial production. Even if the material has superior features, it is not useful unless it is castable. First experiments are conducted in a lab. scale induction furnace shown in Figure 3.2 below.

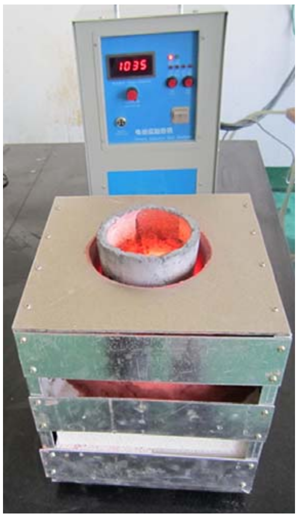

Figure 3.2: High Frequency Induction Furnace.

100 - 150 grams of samples have been prepared in the furnace. There are two main crucible to be used for smelting. One of them is used in induction furnace to smelt iron, the other one is used for alloying liquid metal with aluminum. Alloying crucible is also used for magnesium treatment process. It is needed for making the spheroidal shape graphite in the microstructure. The only disadvantage of lab. scale casting is that cooling is not achieved in a controlled manner. As a result of micro-scale casting experiments, it is proved that aluminum containing High Si-Mo cast irons can be casted flawlessly. After the micro-scale casting, Casting of AlSiMo alloys are performed in Demirsoy Foundry which has a medium frequency induction furnace. 300 kilograms of alloys, which have a different aluminum composition are casted. After sand casting, products are slowly cooled down in sand molds. Finally, chemical composition analysis are performed by Optic Emission Spectrometry and X-ray Florescence technique.

According to the casting results, it is decided that experiments will be continued with three remarkable compositions. These are shown in Table 3.1. Sample names indicate increasing of aluminum content systematically.

Table 3.1: Chemical Composition of AlSiMo Alloys used in experiments.

Sample Name	Fe	Al	Si	Mo	C
AL0	Balanced	0 wt%	** wt%	** wt%	** wt%
AL3	Balanced	** wt%	** wt%	** wt%	** wt%
AL4	Balanced	** wt%	** wt%	** wt%	** wt%

3.2 Microstructural Analysis

In this section, Optic microscope(OM) and scanning electron microscope(SEM) equipped with energy-dispersive spectroscopy(EDS) are used for microstructure characterization. The studied materials are AlSiMo cast iron alloyed with different aluminum content described in Table 3.1. As can be seen in Figure 3.3(c), 3.3(d) the microstructure of aluminum containing alloys are showing compacted graphite distributed in a ferritic matrix. Graphites in the iron matrix are elongated and randomly distributed just like in grey iron, but they are shorter and thicker, and also have rounded edges. They appear as individual worm-shaped. Unlike the microstructure of aluminum containing High Si-Mo, the microstructure of aluminum free cast alloy(AL0) is showing imperfect spheroidal graphite [16] in the iron matrix. it is obviously determined that addition of aluminum in High Si-Mo irons affects the graphite shapes in the iron matrix. There might be several reasons to change microstructure such as carbon content, casting procedure etc. which however, were not observed in this work.

When comparing with the microstructure of High Si-Mo iron and AlSiMo alloys, the graphite size is smaller in the AlSiMo alloys because of the carbon content.

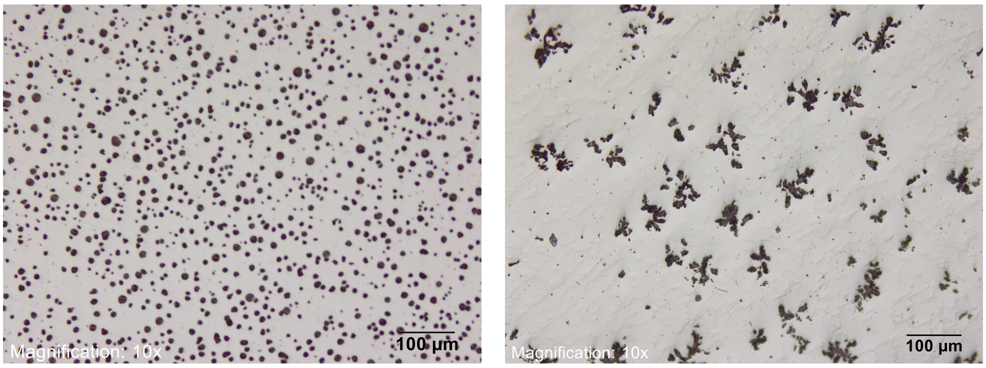

(a) Microstructure of High Si-Mo Ductile Iron.

(b) Microstructure of aluminum free AlSiMo Alloy.

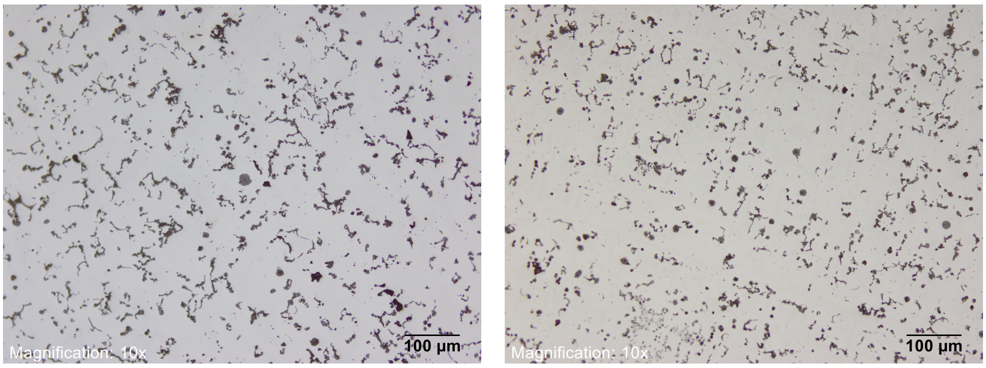

(c) Microstructure of AL3 AlSiMo Alloy.

(d) Microstructure of AL4 AlSiMo Alloy.

Figure 3.3: Optic Microscope Images of High SiMo & AlSiMo Alloys.

When etching the samples with 2 % nitel solution, dendrites are observed in the microstructure of studied alloys characterized by scanning electron microscope. This could result in cooling condition after the casting. Additionally, M_6C(M = Mo or Si) type carbides calculated by computationally are not detected in the microstructure. It is suggested that the size of carbides precipitates is very small to observed, and the resolution of microscope is not sufficient.

According to the EDS results, when the dendrites are observed in detail, it is demonstrated that the aluminum content in the dendrite is more than the ferrit matrix. A region where graphite and dendrites can be seen together, when a line scan is performed indicated arow direction. It is clearly seen in Figure 3.5(a) and 3.5(b).

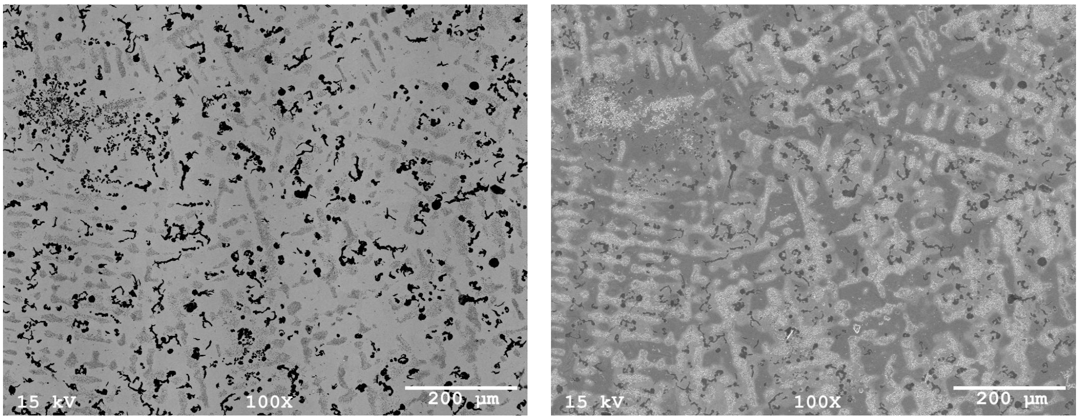

(a) Back-scattered electron image of AlSiMo Alloys.
(b) Secondary - electron image of AlSiMo Alloys.

Figure 3.4: Micrograph images showing the etched (Nital 2%) microstructure of AlSiMo.

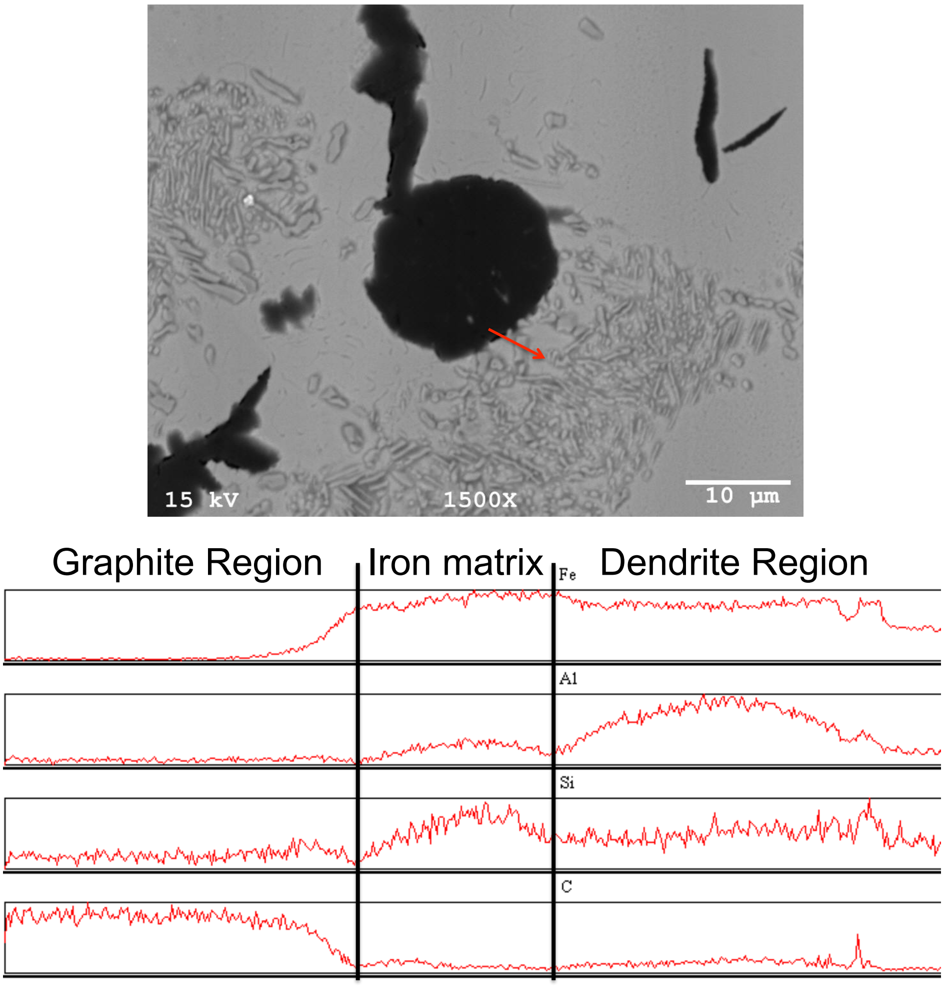

Figure 3.5: Line scan for energy-disperse spectroscopy in microstructure of AlSiMo Alloy.

3.3 Thermogravimetric and Differential Thermal Analysis

Thermogravimetric & differential thermal analysis are performed for determining the A1 temperature of AlSiMo alloys with addition of aluminum. 20 milligrams of samples are used in this measurements. During the analysis, there are two signals, which are weight loss/gain (TG curve), and heat flow/rate(DTA curve), to record. TG curve can be used to extract an information on changes in sample weight, thermal stability, and kinetic parameters for chemical reactions in the samples. Derivative of the measured weight gain/loss curve can be used to reveal if there is any weight lost of the relevant material.

In the differential thermal analysis, studied sample and inert reference sample are conducted identical thermal cycles, and then any temperature difference between sample and reference is recorded. After the measurement, differential temperature is plotted against time. The peak direction shows us if the reaction is endothermic (↓) or exothermic (↑). The phase transitions are always endothermic reaction. The peak orientation is downward.

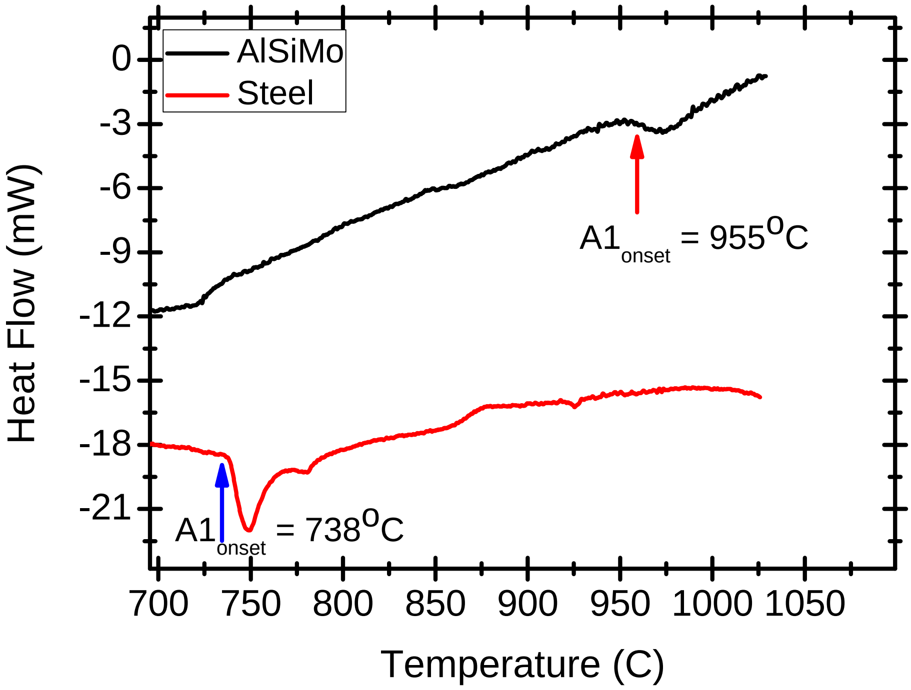

Figure 3.6: Differential Thermal Analysis Result of AL3 sample.

As can be shown in Figure 3.6, Low carbon steel is used as a reference to compare with aluminum containing high Si-Mo iron. Downward peak indicates the endothermic

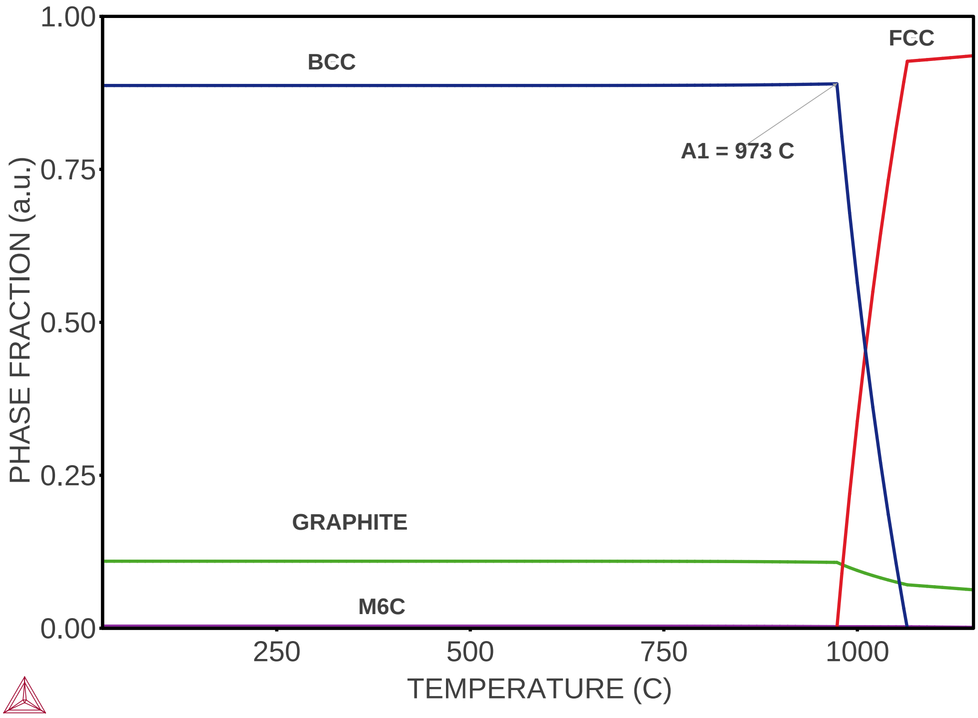

Figure 3.7: Calculated A1 Temperature of AL3 sample.

reaction and it is stated that phase transformation begins at 738^oC and 955^oC for low carbon steel and AlSiMo alloy, respectively. These are the onset values. In Figure 3.7, it is seen that the phase transition begins at 973^oC. It is also known that the A1 temperature for low carbon steel is 723^oC according to metastable Fe-C phase digram. When compering to calculated and measured A1 temperatures for Low carbon steel and AlSiMo alloy, it is obviously shown that calculated value is in good agreement with measured A1 temperature. The percentage error is approximately 2 %. The accuracy of these calculations are proven by this measurement. Consequently, with the addition of aluminum, the A1 temperature in Fe-C phase diagram is shifted to higher temperature.

3.4 High Temperature Oxidation Test

One of the most important material properties is high temperature oxidation resistance for exhaust manifolds due to operating at very high temperature condition. Additionally, they are not actively chilled. For this reason, high temperature oxidation test of AlSiMo alloys is conducted at elevated temperatures.

Test samples are cut fromm as-cast ingots. Coupons with size of approximately 15 x 10 x 5 mm are prepared for the oxidation test conducted in air. For each AlSiMo alloys, ten replicate samples are used. Totally 30 samples are employed for each oxidation condition. After the cutting, test samples are ground with SiC paper down to a finish of 800 grit, and then they are ultrasonically cleaned with acetone for 15 minutes, washed with alcohol.

Oxidation test in ambient condition is performed in a chamber furnace at 750^oC and 850^oC for 96 hours. Before the tests, weight of samples are noted for calculating the weight gain or loss during the test period. Oxidized samples are checked in certain periods and recorded weight due to the forming oxide scale on the material surface. Weight Gain results are given in Figure 3.8(a), 3.8(b).

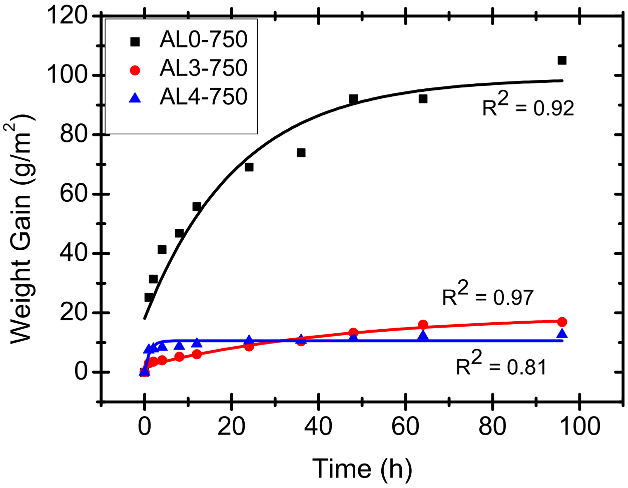

(a) Oxidation Behavior of AlSiMo Alloys at 750^oC.

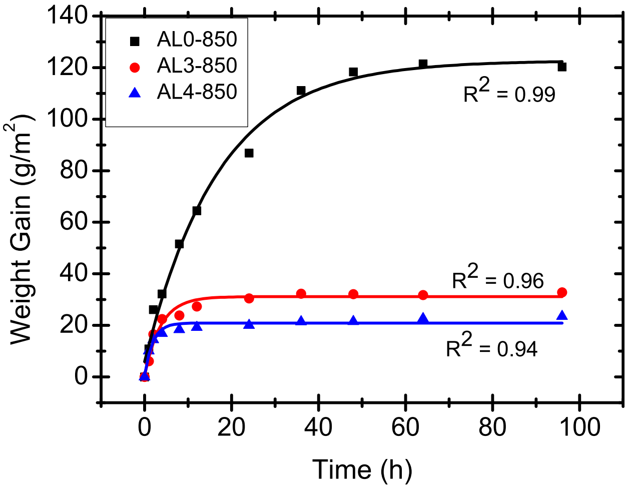

(b) Oxidation Behavior of AlSiMo Alloys at 850^oC.

Figure 3.8: Results of Weight Gain Measurements at Elevated Temperatures.

After the oxidation tests, samples are shown in Figure 3.9.

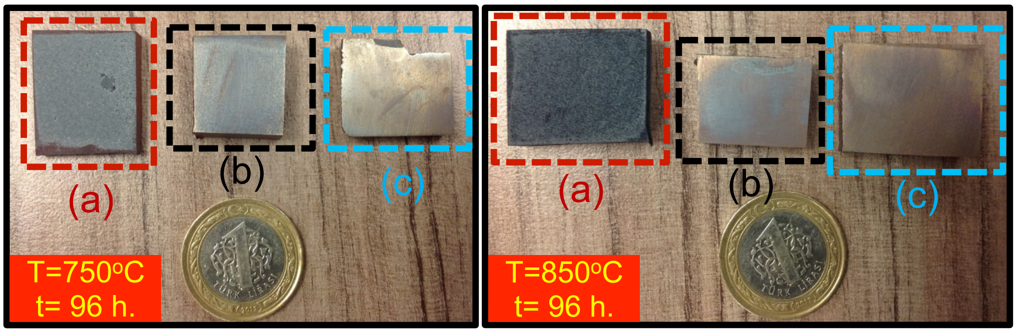

Figure 3.9: Oxidized samples at elevated temperatures. (a) represents to AL0, (b) to AL3 and (c) represents to AL4 alloy.

Aluminum free samples(AL0) has a thick oxide scale while the others are bright and have thin oxide layer. According to the weight gain results, shown in Figure 3.8(a), 3.8(b) it is recognized that why AL0 samples are more opaque. It is shown in weight gain plot that oxidation resistance of aluminum containing High Si-Mo cast irons are more dense which act as a barrier against to oxygen diffusion.

Oxidized AlSiMo alloys at 96 hours are characterized by thin-film x-ray diffraction technique to determine oxide phases grown on the sample surface.

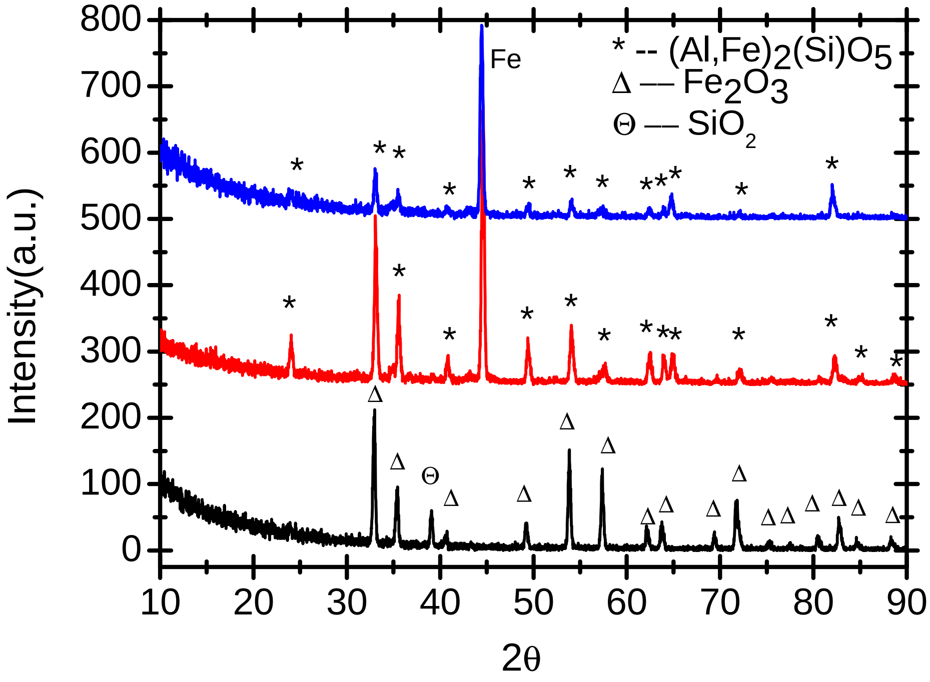

Figure 3.10: Thin Film XRD Results of AL0, AL3 and AL4 are represented, respectively. Colors indicate the different alloys. First, black one is AL0, blue one is AL3 and red indicates the AL4.

In the first sample, aluminum free High Si-Mo, it is observed that hematite, Fe_2O_3, quartz SiO_2 peaks are visible, and also some glassy structure is detected in low angles. However, in the aluminum containing samples, the main peaks are aluminasilicates(Al_2SiO_5) and ironaluminates(Fe_2AlO_5). These two phases formed a solid solution in the lattice so that peak positions are seen nearly the same as hematite peak positions, but it is not. As can be shown obviously in Figure 3.11, and 3.12. Shifted peaks are clearly determined to compare with reference hematite peak positions. Addition to this, as can be seen in Figure 3.12 peak in 64^o splits two different peaks in aluminum containing High Si-Mo alloys. Based on these results, it could be claimed that AlSiMo alloys XRD peaks are different from High Si-Mo cast irons, and these are $(Al,Fe)_2(Si)O_5$ solid solution oxide phases.

However, since kinetic properties of the elements are not taken into consideration, the real oxide scales may conflict with the calculated scale structures by Thermo-Calc.

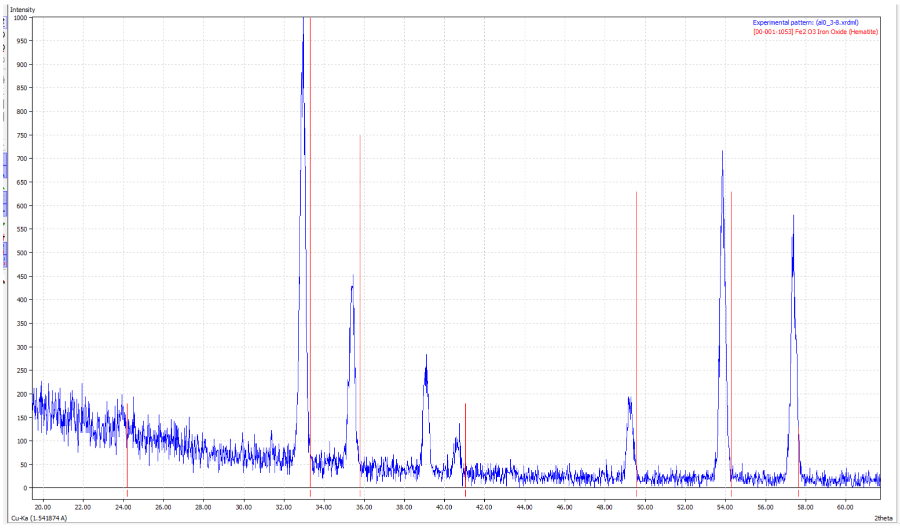

Figure 3.11: XRD Pattern for aluminum containing High Si-Mo Cast Iron. Vertical red lines indicate hematite peak positions.

Furthermore, amorphous content increases with the addition of aluminum. It is figured out from the XRD pattern that peak intensities decrease gradually, while increasing the aluminum content. Finally, iron substrate peaks are apparent in AlSiMo alloys because of the thin oxide film.

Second characterization technique for oxide scale and phases is glow discharge optic emission spectroscopy(GDOES). Basically, the discharged is applied between anode and cathode, that leads to a surface abrasion [30]. Emitted atoms are excited by argon ions, and for a while come back to their fundamental energy level, while giving a characteristic photon. Emitted photons are collected by a photomultiplier, that gives the elemental composition of a material.

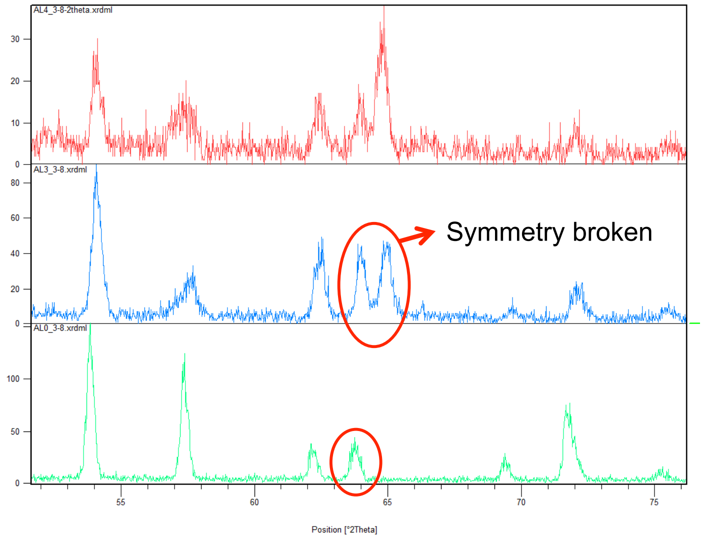

Figure 3.12: XRD Patterns for all three samples, AL0, AL3 and AL4, respectively.

Oxidize AlSiMo alloys (AL3 and AL4) are characterized by GDOES for detecting oxide scale. Measurements are performed to 5 miunutes and it is obtained from the results that selective diffusion and oxidation of aluminum occurs at the surface. And this oxide scale consists of aluminum, iron, silicon and oxygen. Besides, the oxide scales are determined from the GDOES results.

As can be seen in Figure 3.13(d), with the increasing of aluminum content and process temperature, aluminum atoms tend to selectively diffuse on surface to form aluminum rich oxide layer.

Furthermore, SEM / EDS measurements are also performed on the cross section of oxidized samples for the cross-check of oxide scales and oxide phases. For the investigation of oxide phases from the cross-section, oxide surfaces are covered with two-component epoxy paint, and then dried in furnace at 120^oC for 15 minutes. Afterwards, samples are cut the middle of surface. Finally, the cross-section of samples are ground with SiC paper down to a finish of 1200 grit. Oxide thickness of six samples are investigated by using SEM. The results are seen in Figure 3.16. It is demonstrated that aluminum forms a thin, heat resistant and a dense oxide layer which blocks the oxygen diffusion inside the bulk.

When focusing on the AL0 samples, oxide scale is very thick and also consists of two main phases shown in Figure 3.14. Upper layer is iron rich side and the other layer between metal and iron rich oxide phase is silicon rich part. These results is identical to

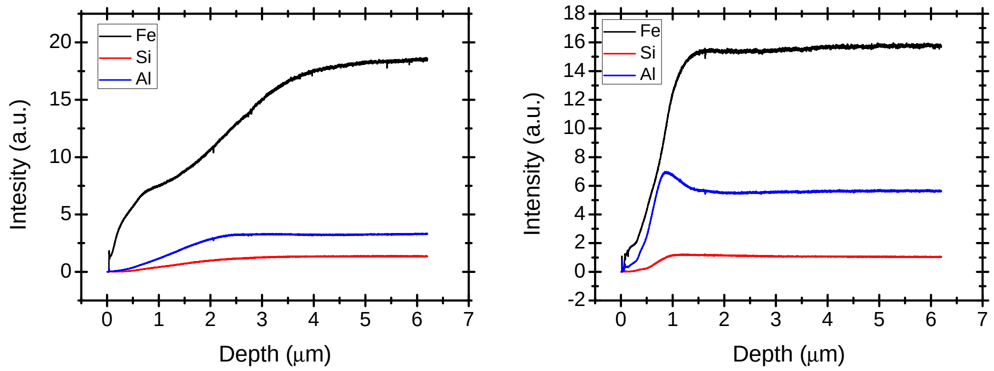

(a) GDOES data for AL3 oxidized at 750^oC. (b) GDOES data for AL4 oxidized at 750^oC.

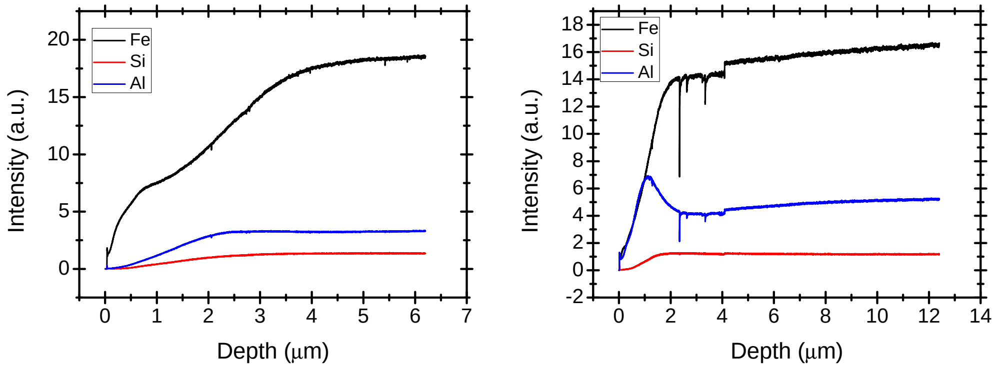

(c) GDOES data for AL3 oxidized at 850^oC. (d) GDOES data for AL4 oxidized at 850^oC.

Figure 3.13: GDOES Results of AlSiMo Alloys at elevated temperature. Colors indicate the elements in the oxide scale.

the ones in literature [31], [32], [33], [34], [35]. The 16 μm thick oxide is quite porous as seen on the cross-section in 3.14. The inner oxide is 14 μm thick. It consisted of a fine distribution of Si-rich Fe oxide. According to Norell et. al study [31], there is a thin SiO_2 layer on metal and oxide interface, but it is reported that the quartz thin layer are not continues.

The element content of the oxide phase can be determined based on the energy disperse spectroscopy data shown in Table 3.2.

Table 3.2: EDS Results for AL0 Sample.

Elements	Fe Oxides	Fe - Si Oxides
Fe	78 wt %	64 wt %
Si	0.34 wt %	10 wt %
O	30 wt %	25 wt %

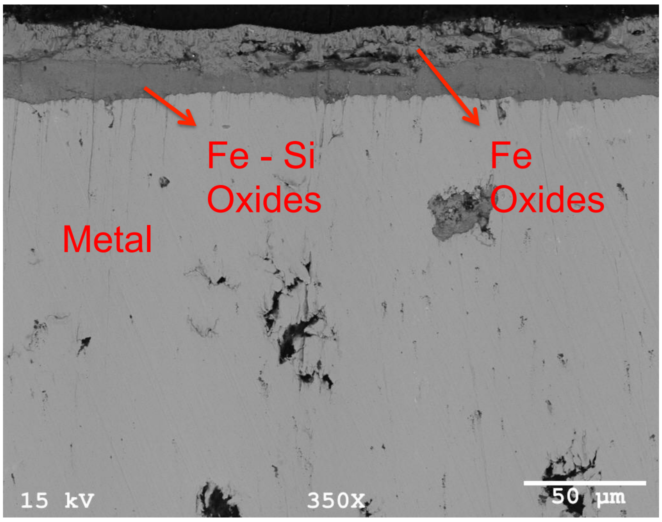

Figure 3.14: SEM image of aluminum free AlSiMo alloy. Cross sectional view.

The other significant EDS result is oxidized aluminum containing samples. As mentioned before, thin and dense oxide scale are grown on surface. Like aluminum free sample, AlSiMo alloys have multilayer oxide scale.

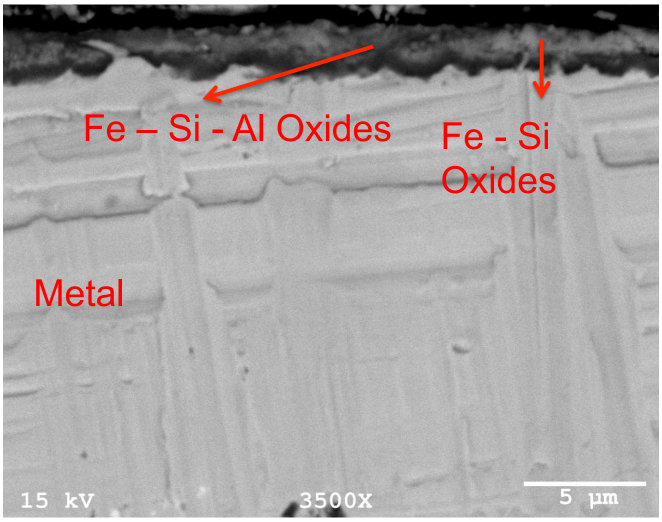

Figure 3.15: SEM image of AL3 AlSiMo alloy. Cross sectional view.

Results proved the weight gain, XRD and GDOES measurements. All characterization results for detecting oxide scale and phases are identical with each other. As can be shown in Figure 3.15, Fe-Si Oxide film is probably discontinued.

Table 3.3: EDS Results for AL3 Sample.

Elements	Fe - Si - Al Oxides	Fe - Si Oxides
Fe	62.92 wt %	66.20 wt %
Si	2.92 wt %	14 wt %
Al	6.73 wt%	0.33 wt%
O	27 wt %	18 wt %

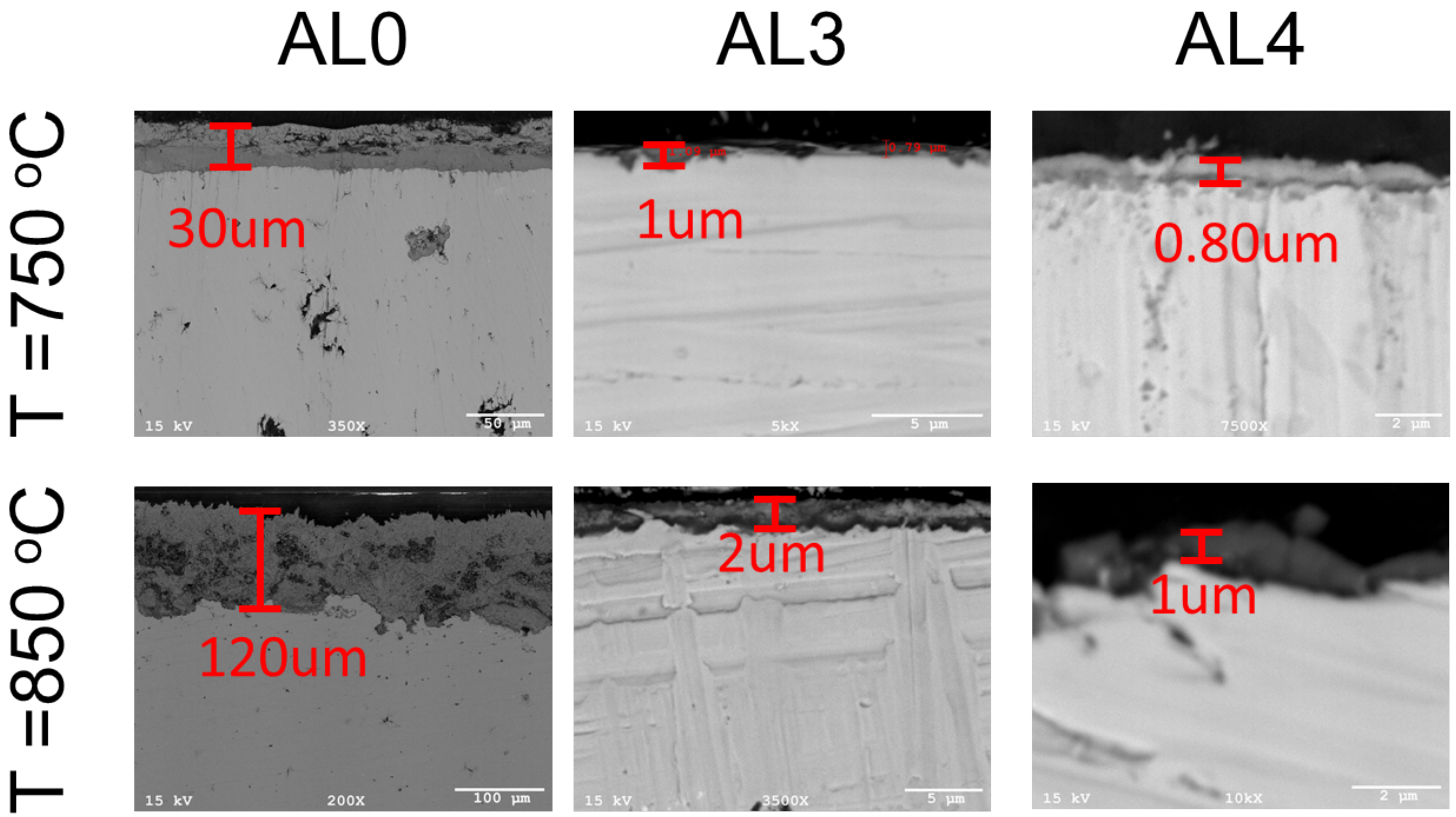

Figure 3.16: Oxide thickness of AlSiMo Alloys and High Si-Mo Iron.

3.5 Thermal Fatigue Test

Thermal fatigue tests are performed at 850^oC with three samples which are High Si-Mo(AL0), and aluminum containing High Si-Mo (AL3 and AL4.). Sample preparation is the same as before. After metallographic process, the test is conducted into a tube furnace and samples are heated to maximum 850^oC in 90 minutes. After holding for 8 minutes, the heated samples are quenched into water. The water temperature is always about 23^oC. The samples are put into furnace again after cooling process. The cycles are performed until cracking on the surface or oxide spallation is observed. Total cycle time is nearly 10 minutes.

Figure 3.17: Photographs of samples after different thermal cycles at 850^oC. AL0 = 41 cycle, AL3 = 51 cycle and AL4 = 75 cycle are shown in above, respectively.

High Si-Mo sample has black colored oxide scale and the sample surface is more porous. On the other hand, AL3 and AL4 samples have grey colored oxide and seem bright. After 15^{th} cycle, oxide film on High Si-Mo sample spalled locally. However,any significant change on the surface of aluminum containing samples is observed.

It is stated that thermal cracks initiated on the surface of AL0 sample, after $41^{th}cycle$. Test results and crack initiation cycles for each compositions are presented in Table 3.4.

According to the literature, the thermal cracks seemed to be in zig-zag shape. Most of them formed in the center of sample's surface and expanded to the edges [36]. The microstructure of the crack region is presented in Figure 3.18(a). It is clearly seen

Table 3.4: Thermal cracks initiation cycles for each compositions.

Sample Name	Crack Initiation Cycle
AL0	41
AL3	51
AL4	75

that microcrack, which is observed on surface of AL3 after 51^{th} cycles, shows typical thermal fatigue crack behaviors.

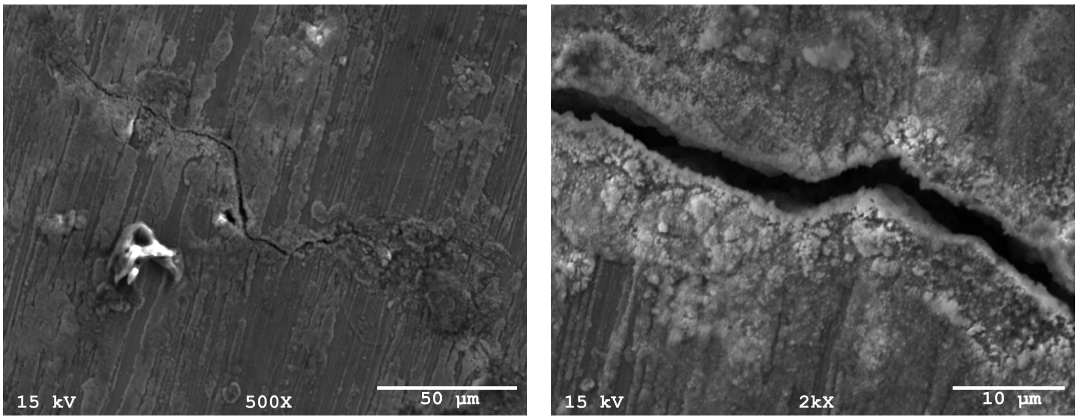

(a) Cracks seems to be in zig-zag or s shape.

(b) Secondary Electron Image of thermal fatigue crack.

Figure 3.18: SEM images of Thermal Fatigue Crack on AL3 surface after 51 cycle.

3.6 Microhardness Measurements and Mechanical Behaviors

In this section, Results of vickers microhardness measurements of AlSiMo alloys are presented and discussed. Indentation method was initiated to measure the hardness and elastic modulus of a material from indentation load - displacement data acquired one cycle loading and unloading [37].

Vickers Hardness number is calculated as follow in Equation 3.1

$$HV = \frac{F2\sin(\frac{136^o}{2})}{d^2} \tag{3.1}$$

The tests are performed under 500mN load for 25 points in each samples. After measurements, acceptable data with reliable curves are obtained, and then average of hardness values, and elastic modulus of alloys are evaluated. Calculated values are shown in Table 3.5.

Hardness value and Tensile strength are increasing with Aluminum content, but the elasticity modules of samples does not change significantly.

Table 3.5: Mechanical Behaviors of AlSiMo Alloys. UTS values are approximate values.

Sample Name	Hardness (HRV)	Elasticity Modulus(GPa)	UTS (MPa)
High Si-Mo [15]	220	170	601
AL0	360	115	900*
AL3	390	148	1055*
AL4	420	150	1150*

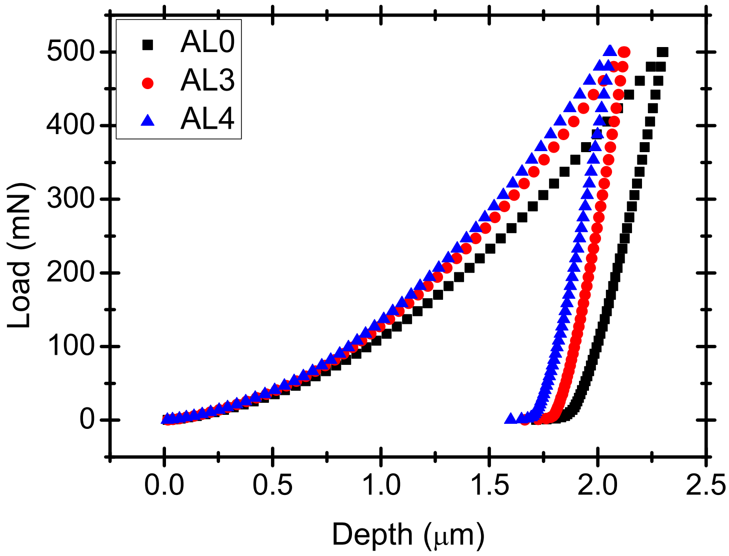

Figure 3.19: Average load and displacement curve for each compositions.

3.7 Accelerated Corrosion Test

Final section of this chapter is accelerated corrosion test. The test is a standardized test method used to check corrosion resistance of coated surface and metallic materials. It is mostly used technique due to the fact that it is inexpensive, fast, repeatable and well systematized.

The accelerated corrosion tests or salt spray testing are conducted for 24 hours. 3.5 % NaCl solution are sprayed continuously on samples under the neutral pH and 35^oC. The samples are constantly wet, and therefore, constantly subject to corrosion. Addition of aluminum improves the corrosion resistance.

Visible improvement was observed with the increment of aluminum content. It is clearly seen in Figure 3.20.

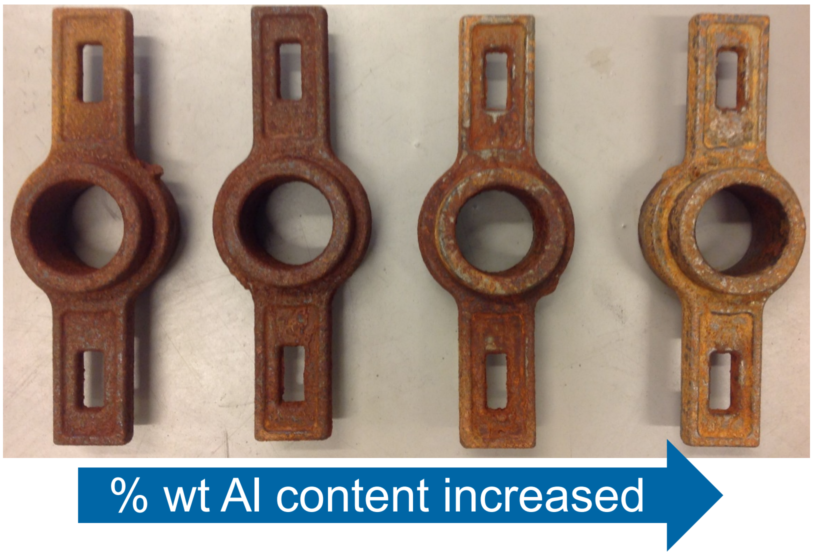

Figure 3.20: Accelerated Corrosion Test Results.

4. CONCLUSION

In this study, aluminum containing High Si-Mo irons which are also called AlSiMo alloys in the context, are investigated by computationally and experimentally. The main conclusions of the study on new generation Fe-based Al-Si-Mo Alloys for exhaust manifold applications are given below:

- High temperature oxidation and thermal fatigue resistance of High Si-Mo ductile iron are improved by adding aluminum in High Si-Mo ductile iron.
- By adding aluminum to the High Si-Mo cast iron, temperature of eutectoid phase transformation (A1) in the Fe - C system is increased.
- It is stated that thermodynamic properties of AlSiMo alloys(i.e. heat capacity, thermal expansion, density, volumetric change depends on temperature etc.) obtained from calculations, are better than High Si-Mo ductile iron.
- Decrease in density provides a weight reduce of 5 to 10 % which can lead to the manufacture of light weighted designs.
- Calculation results are in good agreement with experiments.
- It is observed that the microstructure of AlSiMo alloys is compacted graphite iron, which is an outstanding advantage that leads to the new design of cylinder head with integrated exhaust manifolds. Using this type of integrated casting enable to fabricate very compact components.
- Weight gain results show that the oxidation resistance of AlSiMo alloys is 6 times better than the High Si-Mo cast iron.
- Selective diffusion and oxidation of aluminum at the surface is observed which improves the oxidation resistance of AlSiMo alloys.

- Instead of hematite oxide scale, dense aluminasilicate and ironaluminate films are found in the surface of AlSiMo alloys. These dense oxide films increase the heat resistance of material.

- Aluminum containing High Si-Mo alloys exhibit more thermal fatigue resistance than High Si-Mo cast irons.

- Additionally, improvement on electro-chemical corrosion resistance is obtained with the addition of aluminum in High Si-Mo cast iron.

5. OUTLOOK

Although the computational and experimental data and discussion presented in this work explain the optimization of chemical composition of AlSiMo alloys, high temperature oxidation resistance and thermal fatigue resistance, further work is needed.

Laser Flash Test will be performed for determining the thermal conductivity with respect to temperature. Since the thermal conductivity decreases when increasing temperature, this leads to high temperature gradient and it could create residual tensile stresses so this residual tensile stresses accelerate the growth rate of thermal fatigue crack.

As reported on this study, creep is one of the most important failure mechanisms for hot end exhaust systems. Thus, Creep test and cyclic plasticity measurements are needed to be conducted at elevated temperatures.

Finally, before the casting of AlSiMo exhaust manifolds, finite element analysis is needed to be performed in the light of this experimental and computational results.

REFERENCES

[1] **Yamagata, H.**, (2005). The science and technology of materials in automotive engines, CRC, Cambridge, 1. edition.

[2] **Smith, T.J., Maier, H.J., Sehitoglu, H., Fleury, E. and Allison, J.** (1999). Modeling High-Temperature Stress-Strain Behavior of Cast Aluminum Alloys, *Metallurgical and Materials Transactions A*, 133–146.

[3] **Gocmez, T. and Deuster, U.** (2009). An Integral Engineering Solution for Design of Exhaust Manifolds, *SAE Technical Paper*, Detroit, United States of America.

[4] **Neu, R.W. and Sehitoglu, H.** (1989). Thermomechanical Fatigue, Oxidation, and Creep: Part I. Damage Mechanisms, *Metallurgical Transactions*, 1755–1767.

[5] **Zhuang, W.Z. and Swansson, N.S.** (1998). Thermo-Mechanical Fatigue Life Prediction: A Critical Review.

[6] **Neu, R.W. and Sehitoglu, H.** (1989). Thermomechanical Fatigue, Oxidation, and Creep: Part II. Life Prediction, *Metallurgical Transactions*, 1769–1781.

[7] **Su,vX., Zubeck, M., Lasecki, J., Sehitoglu, H., Engler-Pinto, C., Tang, C. and Allison, J.**, (2002). Thermomechanical Fatigue Analysis of Cast Aluminum Engine Components, ASTM International, West Conshohocken, 1. edition.

[8] **Stolarz, J.** (2003). Fatigue short crack behaviour in metastable austenitic stainless steels with different grain sizes, *LCF 5*, Berlin, Germany.

[9] **Lia, G.Y.**, (1990). High Temperature Oxidation and Corrosion of Metals, ASM International, New York, 1. edition.

[10] **Young, D.J.**, (2008). High-Temperature Corrosion of Engineering Alloys, Elsevier, Cambridge, 1. edition.

[11] **Gaskel, D.**, (2003). Introduction to the Thermodynamics of Materials, Taylor and Francis, New York, 4. edition.

[12] **Stott, F.** (1987). The protective action of oxide scales in gaseous environments at high temperature, *Reports on Progress in Physics*, 861.

[13] **Chang, Y.N. and Wei, F.I.** (1989). High temperature oxidation of low alloy steels, *Journal of Materials Science*, 14–22.

[14] **Birks, N., Meier, G. H. and Pettit, F.S.**, (2006). Introduction to the High Temperature Oxidation of Metals, Cambridge Univ. Press, Cambridge, 4. edition.

[15] **SAE-J2515** (1999). High Temperature Materials for Exhaust Manifolds, *Society of Automobile Engineers*.

[16] **Steiner, R.**, (1993). Properties and Selection: Irons, Steels, and High-Performance Alloys, ASM International, New York, 2. edition.

[17] **Durand, M.**, (2003). Microstructure of Steels and Cast Irons, Springer, New York, 1. edition.

[18] **Ekstrom, M.** (2013). Development of a Ferritic Ductile Cast Iron For Increased Life in Exhaust Applications, *Ph.D. thesis*, Royal Institute of Technology, Stockholm.

[19] **Liu Z. K.** (2009). First Principles Calculations and CALPHAD Modeling of Thermodynamics, *Journal of Phase Equilibria and Diffusion*, 25–30.

[20] **Saunders, N. and Miodownik, A.P.**, (1998). CALPHAD Calculation of Phase Diagrams, Pergamon Materials Series, New York, 1. edition.

[21] **Kaufman, L., Bernstein, H.**, (1970). Computer Calculation of Phase Diagrams, Academic Press, New York, 1. edition.

[22] **Solak, N.** (2007). Interface Stability in Solid Oxide Fuel Cells for Intermediate Temperature Applications, *Ph.D. thesis*, Max-Planck Institute, Stuttgart.

[23] **Hillert, M.** (1981). Some viewpoints on the use of a computer for calculating phase diagrams, *Physica B*, 31–40.

[24] **Lukas, H.L, Weiss, J. and Henig, E.** (1982). Strategies for the calculation of phase diagrams, *CALPHAD*, 229–251.

[25] **Andersson, J. O., Helander,T., Hoglund, L., Shi,P. and Sundman, B.** (2002). Thermo-Calc and DICTRA, computational tools for materials science, *CALPHAD*, 273–312.

[26] **Kattner, U.R. and Campbell, C.E.** (2009). Modelling of thermodynamics and diffusion in multicomponent systems, *Materials Science and Technology*, 443–458.

[27] **Dinsdale, A.** (1991). SGTE data for pure elements, *CALPHAD*, 317–425.

[28] **Connetable, D., Lacaze, J., Maugis, P. and Sundman, B.** (2008). A Calphad assessment of Al-C-Fe system with the K carbide modelled as an ordered form of the fcc phase, *CALPHAD*, 361–370.

[29] **Lu, X.G., Selleby, M. and Sundman, B.** (2005). Implementation of a new model for pressure dependence of condensed phases in Thermo-Calc, *CALPHAD*, 49–55.

[30] **Url-1**, `http://www.analyses-surface.com`.

[31] **Tholence, F. and Norell, M.** (2008). High Temperature Corrosion of Cast Alloys in Exhaust Environments I-Ductile Cast Irons, *Oxid Met*, 13–36.

[32] **Lin, M. B., Wang, C. J. and Volinsky, A.A.** (2011). High Temperature Oxidation Behavior of Flake and Spheroidal Graphite Cast Irons, *Oxid Met*, 161–168.

[33] **Ekstrom, M., Szakalos, P. and Jonsson, S.** (2013). Influence of Cr and Ni on High-Temperature Corrosion Behavior of Ferritic Ductile Cast Iron in Air and Exhaust Gases, *Oxid Met*, 455–466.

[34] **Chandrambhorn, S., Thublaor, T. and Pongpankasame, J.** (2013). High Temperature Oxidation of Al-alloyed SiMo Cast Iron in CO_2-containing Atmospheres, *Advanced Materials Research*, 132–135.

[35] **Dawi, K., Favergeon, J. and Moulin, G.** (2008). High temperature corrosion of the Si-Mo cast iron in exhaust atmosphere, *Materials Science Forum*, 743–751.

[36] **Yang, Y., Cao, Z., Lian, Z. and Yu, H.** (2013). Thermal Fatigue Behavior and Cracking Characteristics of High Si-Mo Nodular Cast Iron for Exhaust Manifolds, *Journal of Iron and Steel Research*, 52–57.

[37] **Oliver, W. C. and Pharr, G.M.** (2003). Measurement of hardness and elastic modulus by instrumented indentation: Advances in understanding and refinements to methodology, *Journal of Materials Research*, 03–20.

CURRICULUM VITAE

Name Surname: Rıfat YILMAZ

Place and Date of Birth: Tekirdag & June 30, 1989

Adress: Istanbul Technical University, Dept. Metallurgical & Materials Eng. Dokum Holu, Maslak / Istanbul

E-Mail: yilmazrif@itu.edu.tr

B.Sc.: Physics Engineering, Istanbul Technical University

PUBLICATIONS/PRESENTATIONS ON THE THESIS

- **Yilmaz R.**, Kondakci E. and Solak N., 2014: Improvement of High Temperature Oxidation and Mechanical Behaviors of High Si-Mo Ductile Iron for Exhaust Manifolds. *SAE World Congress - Oral Presantation*, April 08-10, 2014 Detroit, USA.